ACS NANO

Open Access

www.acsnano.org

ARTICLE

Hydrogel Microneedle Patches Loaded with Stem Cell Mitochondria-Enriched Microvesicles Boost the Chronic Wound Healing

Wen-De Yao,[‖] Jun-Nian Zhou,*[,‖] Chao Tang, Ju-Lei Zhang, Zhao-Yang Chen, Yan Li, Xiao-Jing Gong, Ming-Yi Qu, Quan Zeng, Ya-Li Jia, Hai-Yang Wang, Tao Fan, Jing Ren, Ling-Li Guo, Jia-Fei Xi, Xue-Tao Pei, Yan Han,* and Wen Yue*

Cite This: *ACS Nano* 2024, 18, 26733−26750

Read Online

ACCESS | Metrics & More | Article Recommendations | Supporting Information

ABSTRACT: **Rescuing or compensating mitochondrial function represents a promising therapeutic avenue for radiation-induced chronic wounds. Adult stem cell efficacies are primarily dependent on the paracrine secretion of mitochondria-containing extracellular vesicles (EVs). However, effective therapeutic strategies addressing the quantity of mitochondria and mitochondria-delivery system are lacking. Thus, in this study, we aimed to design an effective hydrogel microneedle patch (MNP) loaded with stem cell-derived mitochondria-rich EVs to gradually release and deliver mitochondria into the wound tissues and boost wound healing. We, first, used metformin to enhance mitochondrial biogenesis and thereby increasing the secretion of mitochondria-containing EVs (termed "Met-EVs") in adipose-derived stem cells. To verify the therapeutic effects of Met-EVs, we established an *in vitro* and an *in vivo* model of X-ray-induced mitochondrial dysfunction. The Met-EVs ameliorated the mitochondrial dysfunction by rescuing mitochondrial membrane potential, increasing adenosine 5′-triphosphate levels, and decreasing reactive oxygen species production by transferring active mitochondria. To sustain the release of EVs into damaged tissues, we constructed a Met-EVs@Decellularized Adipose Matrix (DAM)/Hyaluronic Acid Methacrylic Acid (HAMA)-MNP. Met-EVs@DAM/HAMA-MNP can load and gradually release Met-EVs and their contained mitochondria into wound tissues to alleviate mitochondrial dysfunction. Moreover, we found Met-EVs@DAM/HAMA-MNP can markedly promote macrophage polarization toward the M2 subtype with anti-inflammatory and regenerative functions, which can, in turn, enhance the healing process in mice with skin wounds combined radiation injuries. Collectively, we successfully fabricated a delivery system for EVs, Met-EVs@DAM/HAMA-MNP, to effectively deliver stem cell-derived mitochondria-rich EVs. The effectiveness of this system has been demonstrated, holding great potential for chronic wound treatments in clinic.**

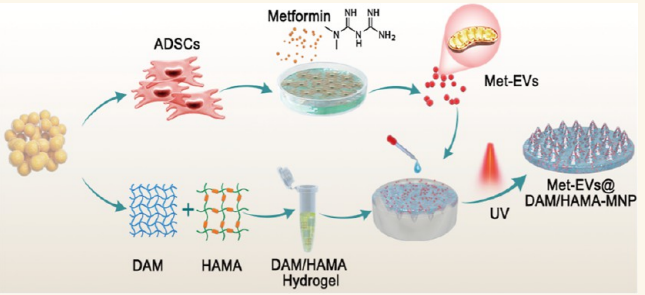

KEYWORDS: *stem cell, metformin, mitochondria-enriched extracellular vesicle, hydrogel microneedle patch, radiation-induced injury*

Radiotherapy for the patients with malignant tumors and nuclear and radiological accidents can lead to the development of irradiation-associated skin injuries. These wounds tend to resist treatment and may be cancerous, causing immense suffering in patients.[1−3] However, the pathological mechanisms that cause radiation-induced injuries are yet to be resolved, and no fully efficacious treatment options exist.[4] Although the cell nucleus has long been considered the main target of radiation damage, increasing evidence supports the notion that mitochondrion is another principal subcellular organelle that is targeted in radiation-induced damage.[2,5,6] Radiation injuries are closely associated with oxidative stress, which occurs when organisms are exposed to radiation-induced damage to mitochondrial macromolecules and the electron transport

Received: May 24, 2024
Revised: August 23, 2024
Accepted: August 26, 2024
Published: September 6, 2024

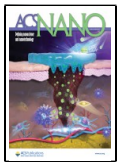

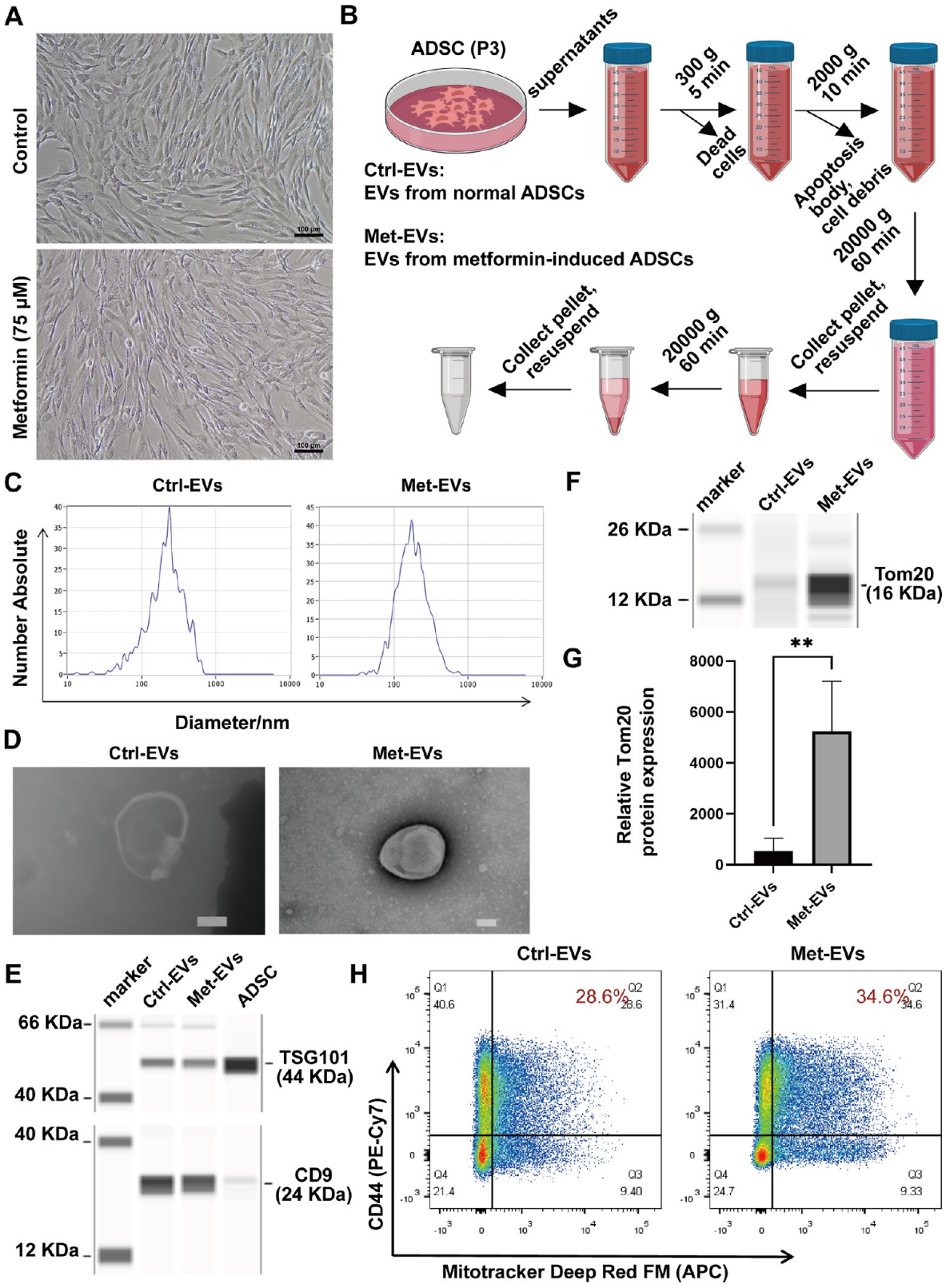

Figure 1. Fabrication and characterization of ADSC-EVs. (A) Morphology of control ADSCs (above) and metformin-treated ADSCs (below) by light microscopy. Scale bar, 100 μm. (B) Flowchart of the isolation of EVs. (C) Nanoparticle tracking analysis (NTA) of the range of particle size distribution of Ctrl-versus Met-EVs. (D) Transmission electron microscopy (TEM) images of Ctrl- and Met-EVs. Scale bar, 100 nm. (E) CD9 and TSG101 expression in Ctrl- and Met-EVs and ADSCs was assessed using capillary immunoassays. (F) Tom20 expression levels in Ctrl- and Met-EVs were evaluated by capillary immunoassays. (G) Capillary immunoassays detected a significant difference in Tom20 expression between Ctrl- and Met-EVs ($n = 4$). (H) Flow cytometric analysis of $CD44^+MTDR^+$ EVs in Ctrl-EVs (28.6%) and Met-EVs (34.6%). $^{**}p < 0.01$. EVs, extracellular vesicles; Met, metformin; Ctrl, control; ADSCs, adipose-derived stem cells.

https://doi.org/10.1021/acsnano.4c06921
ACS Nano 2024, 18, 26733−26750

chain.[7] This exposure results in the generation of primary and secondary reactive oxygen species (ROS) and in mitochondrial dysfunction,[7−9] leading to a prolonged inflammatory phase in the wound, delayed wound healing, and, ultimately the development of chronic wounds.[10]

Mitochondria transplantation has been hypothesized to improve mitochondrial dysfunction in damaged cells. To achieve better therapeutic effects, transplanted mitochondria must be viable and be capable of respiratory functions. However, one must note that isolated mitochondria remain active for only a short time *in vitro*,[11,12] limiting the potential applications of freshly isolated mitochondria transplantation.[13,14] Extracellular vesicles (EVs) that contain mitochondrial components, especially from stem cells, are capable of transferring healthy mitochondria to damaged tissues, which results in the amelioration of metabolic disorders in injured tissues.[14−18] Mitochondria transported by EVs are preferable over isolated/naked mitochondria because of lipid bilayer protection, which enables convenient storage.[13] Moreover, Ikeda *et al.* demonstrated that mitochondria within EV are more resistant to Ca^{2+} overload and oxidative stress compared to isolated/naked mitochondria.[14] Therefore, the use of mitochondria-containing EVs is a more suitable option for treating skin wounds combined with radiation injuries.

Boosting the number of functional mitochondria in stem cell-secreted EVs can potentially increase the therapeutic effects on wound healing. Metformin, a drug commonly used clinically for treating diabetes, acts as a mitochondrial biogenic agent, promoting the formation of new mitochondria.[19−21] However, whether mitochondria content in secreted EVs could be elevated by metformin remains unknown. Thus, we aimed to evaluate if treatment of adipose-derived stem cells (ADSCs) with metformin can enhance mitochondrial biogenesis and, consequently, the secretion of mitochondria-containing EVs.

Microneedle patch (MNP)-based delivery is a painless, and self-administered technique better than the hypodermic needle. Among four producing approaches of MNPs, hydrogel MNP are preferred for enhanced tissue uptake of EVs and EVs release, because EVs can be encapsulated, stored, and protected in the hydrogel and delivered into the target cells after inserting the skin, followed by the biodegradation process.[22]

Considering that the repair of damaged tissues by EVs requires sustained-release delivery *in situ* to achieve good therapeutic effects, this study aimed to establish an MNP-based delivery system effectively delivering stem cell-derived mitochondria-rich EVs and treat chronic wound healing. In the study, metformin-treated ADSC-derived EVs (Met-EVs) were mixed well together in prehydrogels composed of a decellularized adipose matrix (DAM) and hyaluronic acid methacrylic acid (HAMA), which were then prepared as a MNP to poke the biofilm layer of a wound and gradually release and deliver mitochondria into wound tissues. This process results in improvements of mitochondrial dysfunction, allowing for the effective healing of skin wounds complicated by radiation injuries.

RESULTS AND DISCUSSION

Fabrication and Characterization of Met-EVs. Emerging evidence suggests that the therapeutic effects of MSCs may be mostly because of paracrine EV secretion rather than cell engraftment and differentiation, with the former increasingly becoming an attractive and safer therapeutic source.[23,24] MSC-derived EVs >300 nm in size can reportedly transport functional mitochondria or efficient mitochondrial components to injured cells to reprogram their metabolism and improve cellular respiratory functions,[14−18,25] which distinguishes from somatic pluripotency reprogramming.[26] Notably, O'Brien *et al.*[25] reported that MSCs beyond passage 4 produce fewer mitochondria-containing EVs than do early passage MSCs, which is consistent with our quality standards for clinical-grade MSCs used from passage 3 to 5.[27,28] In the present study, based on the cell growth rate and output of mitochondria-containing EVs, we selected passage 3 ADSCs for further investigation.

We first isolated ADSCs and demonstrated that cultured ADSCs were highly positive for mesenchymal stem cell (MSC) surface markers, including CD29, CD73, CD90, CD105, and CD166, but negative for hematopoietic cell (CD34 and CD45), immune cell (CD14 and CD38), and endothelial cell (CD31) surface markers (see Figure S1A in Supporting Information). ADSCs have trilineage differentiation potential into adipocytes, osteocytes, and chondrocytes, as confirmed by typical staining of Oil Red O, Alizarin Red, and Alcian Blue, respectively, which showed lipid droplets in lipogenically differentiated cell cytoplasms, calcium deposition in the osteogenically differentiated cell cytoplasms, and acidic mucopolysaccharide deposition in the chondrocyte globules of differentiated cells, respectively (Figure S1B). These results suggest that our isolated ADSCs were well-cultured MSCs.

To screen for a suitable drug to increase mitochondrial biogenesis within ADSCs, available reports led us to select two drugs that are commonly used clinically: metformin and pioglitazone. Pharmacological metformin concentrations enhance mitochondrial fission, thereby improving mitochondrial respiration and restoring the mitochondrial life cycle.[29] Pioglitazone increases the copy number of mitochondrial DNA (mtDNA) in cells.[30,31] To investigate whether metformin and pioglitazone affect mitochondrial biogenesis in ADSCs, we first examined the drug dose−effect relationship of metformin and pioglitazone on ADSCs using a CCK-8 assay. The results indicated that the half maximal inhibitory concentration of metformin and pioglitazone on ADSCs were 3143 and 546.7 μM, respectively (Figure S2). MitoTracker Deep Red FM (MTDR) is a fluorescent probe that labels mitochondria in living cells. It selectively accumulates in active mitochondria, and this accumulation is mitochondrial membrane potential (MMP)-dependent; MTDR effectively accumulates and emits fluorescent signals when mitochondria are active and have normal membrane potential.[32] Next, we selected a series of metformin concentrations (0, 25, 50, 75, and 100 μM) and pioglitazone (0, 5, 10, 25, and 50 μM) to treat ADSCs, followed by labeling the mitochondria of ADSCs with MTDR. The mean fluorescence intensity of MTDR expression in ADSCs was analyzed using flow cytometry. The results showed that with the increase of metformin concentration, the expression of MTDR in ADSCs tended to be upgraded, and MTDR reached the peak when the metformin concentration was 75 μM (Figure S3). Furthermore, ADSC morphology was not altered by metformin treatment (Figure 1A).

Next, we compared Met-EVs with EVs from normal ADSCs (Ctrl-EVs). EVs were isolated by differential centrifugation of the supernatants from passage 3 ADSCs (Figure 1B). NTA and TEM showed that the EVs in both groups were between 100−1000 nm in size (Figure 1C), with a typical "cup-shaped" morphological appearance (Figure 1D). We then confirmed the expression of the EV markers CD9 and TSG101 using a capillary-based immunoassay at protein level (Figure 1E).

https://doi.org/10.1021/acsnano.4c06921
ACS Nano 2024, 18, 26733−26750

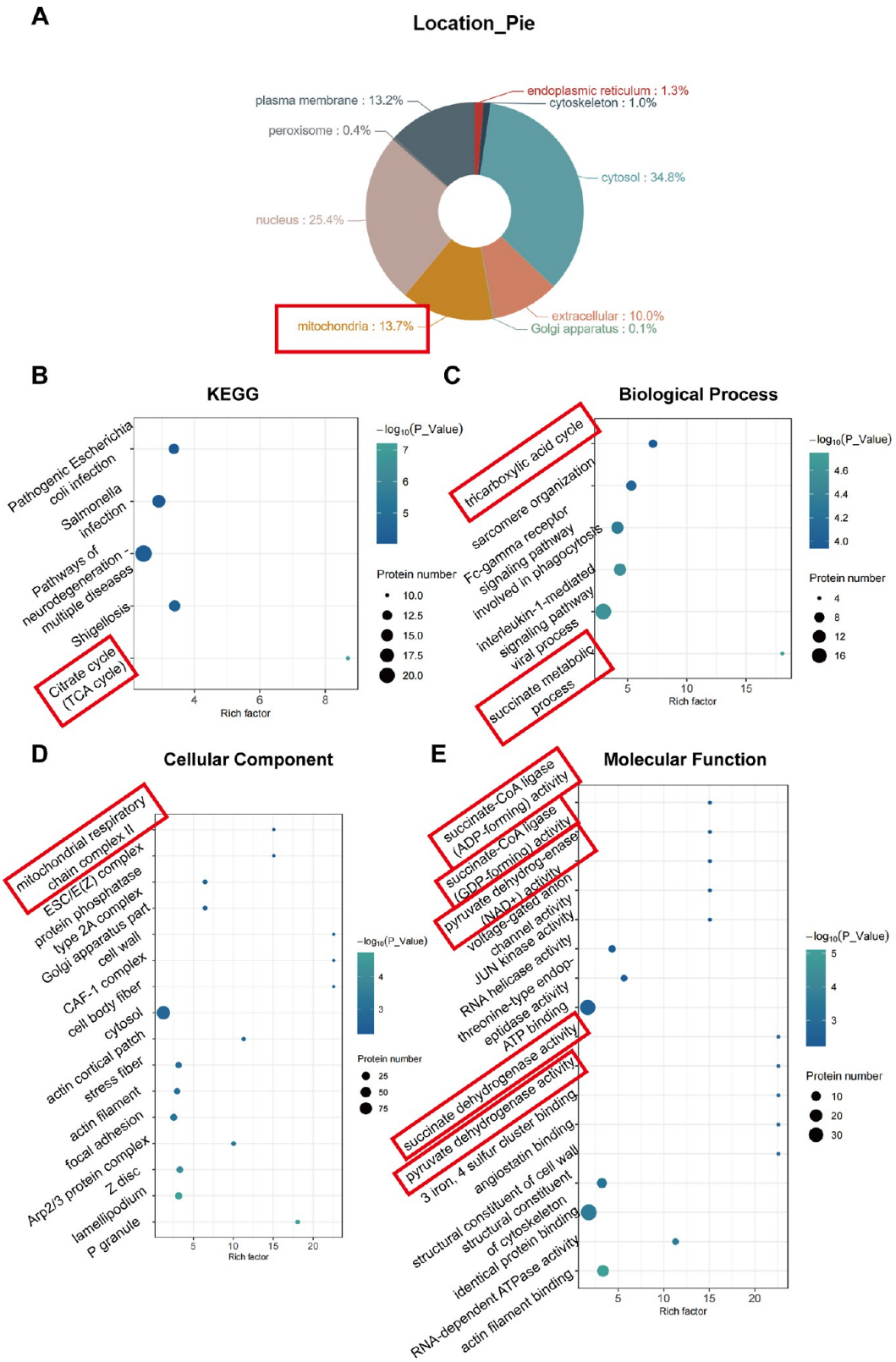

Figure 2. Enrichment analysis of differential proteins between Met- and Ctrl-EVs. (A) Analysis of subcellular localization of differentially expressed proteins. (B) Kyoto Encyclopedia of Genes and Genomes (KEGG) pathway enrichment analysis of the upregulated proteins. (C−E) Gene Ontology (GO) classification of the upregulated proteins in terms of biological processes, cellular components, and molecular functions. Met, metformin; Ctrl, control; EVs, extracellular vesicles; KEGG, Kyoto Encyclopedia of Genes and Genomes; GO, Gene Ontology.

Next, to clarify whether metformin increases the content of active mitochondria in EVs secreted by ADSCs, the expression level of the mitochondrial membrane protein Tom20 in the EVs of the two groups was examined using a capillary-based immunoassay. The results revealed that Tom20 expression levels in Met-EVs were 9.86-fold higher than those in Ctrl-EVs

https://doi.org/10.1021/acsnano.4c06921
ACS Nano 2024, 18, 26733−26750

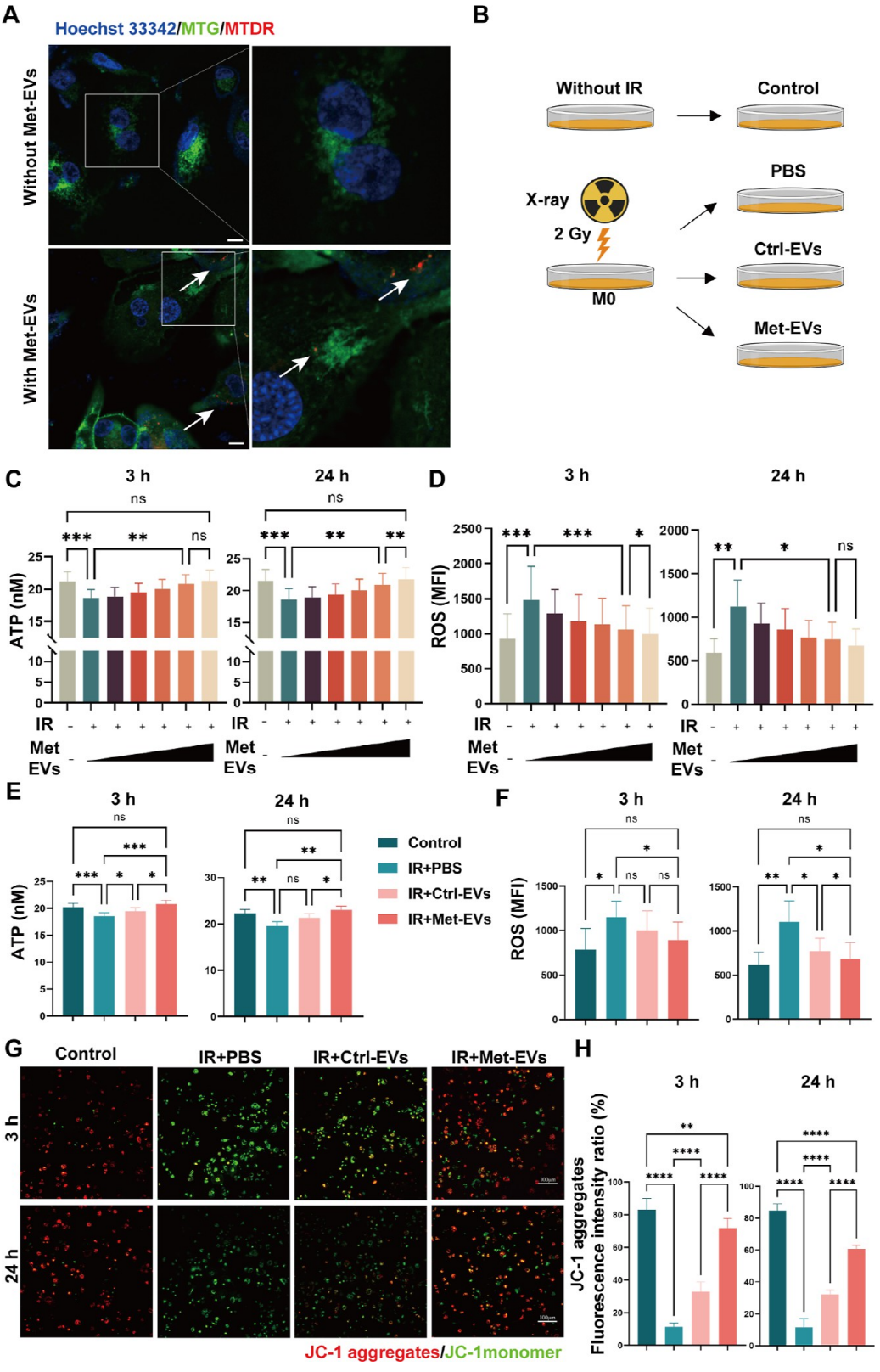

Figure 3. Met-EVs ameliorate X-ray-induced mitochondrial dysfunction in macrophages. (A) Representative microscopic images of MTDR-labeled exogenous mitochondria (red) in macrophages after treatment with Met-EVs. Mitochondria (indicated by white arrows) within the transferred Met-EVs were observed in recipient macrophages prelabeled with MitoTracker Green FM (MTG, green). Scale bar, 10 μm. (B) Schematic diagram of the experimental groups set up for comparison with the groups Without IR, IR + phosphate-buffered saline, PBS, IR + Ctrl-EVs, and IR + Met-EVs. (C,D) ATP and ROS levels in X-ray-injured macrophages treated with Met-EVs. (0, 3.0×10^6, 1.0×10^7, 3.0×10^7, 10^8 or 3.0×10^8 particles/mL: wedges). Left: 3 h post-treatment. Right, 24 h post-treatment. (E,F) ATP and ROS levels in X-ray-injured macrophages treated with Met- and Ctrl-EVs at a concentration of 10^8 particles/mL. Left, 3 h post-treatment. Right, 24 h post-treatment. (G) Representative images of MMP determined using a JC-1 kit (JC-1 aggregates, red, bioactive mitochondria; JC-1 monomer, green, impaired

https://doi.org/10.1021/acsnano.4c06921
ACS Nano 2024, 18, 26733−26750

Figure 3. continued

mitochondria) in X-ray-injured macrophages treated with Met- or Ctrl-EVs at a concentration of 10^8 particles/mL. Top panel, 3 h post-treatment; bottom panel, 24 h post-treatment. Scale bars,100 μm. (H) Ratio of JC-1 aggregates (red) to the total intensity of red and green fluorescence (%). Both fluorescence intensities (red and green) were analyzed using ImageJ software. $n = 4-9$, in each group, ns $p > 0.05$, *$p < 0.05$, **$p < 0.01$, ***$p < 0.001$, and ****$p < 0.0001$. Met, metformin; MTDR, MitoTracker Deep Red; EVs, extracellular vesicles; Ctrl, control; IR, irradiation; PBS, phosphate-buffered saline.

(Figure 1F,G). We further analyzed the percentage of active mitochondria-containing Met-EVs using flow cytometry. ADSCs were prestained with MTDR, followed by incubation with an anti-CD44 antibody. The results revealed an increased proportion of $CD44^+MTDR^+$ EVs in Met-EVs compared with that in Ctrl-EVs (see Methods—Flow Cytometric Analysis of EVs, Figures S4, and 1H). These results suggest that ADSC-EVs prepared by differential centrifugation contain active mitochondria and that metformin treatment enhances the percentage of mitochondria-containing EVs.

Increased Mitochondria-Associated Protein Content within Met-EVs. To comprehensively analyze the biological effects of metformin on ADSC-derived EVs, we performed a 4D-label free proteomic analysis of Met- and Ctrl-EVs. We identified 3297 proteins in the EVs of the two groups, among which an expression difference greater than 2-fold (both up- and downregulation) was displayed, and those with a p-value (t-test/significance A) < 0.05 were considered significantly differentially expressed proteins. A total of 219 differentially expressed proteins were identified, comprising 146 upregulated and 73 downregulated proteins (Figure S5). Subcellular localization analysis showed that 13.7% of these proteins were derived from mitochondria (Figure 2A).

We then performed KEGG pathway enrichment of the upregulated proteins. The results showed that the upregulated proteins had the highest degree of enrichment in the tricarboxylic acid cycle pathway (Figure 2B). Furthermore, functional annotation of the upregulated proteins was performed using GO enrichment analysis considering biological processes (Figure 2C), cellular components (Figure 2D), and molecular functions (Figure 2E). The results showed that two of the top six enriched pathways in biological processes were involved in the succinate metabolic process and tricarboxylic acid cycle pathway, which is associated with mitochondrial metabolism (Figure 2C). One of the top 16 most enriched pathways in cellular components, mitochondrial respiratory chain complex II, is involved in mitochondrial metabolism (Figure 2D). Five of the 16 most enriched molecular functions, pyruvate dehydrogenase (acetyl-transferring), succinate dehydrogenase (ubiquinone), pyruvate dehydrogenase (NAD^+), succinate-CoA ligase (GDP-forming), and succinate-CoA ligase (ADP-forming), are associated with mitochondria (Figure 2E).

Taken together, these results suggest that EV-transported proteins associated with mitochondrial metabolism are upregulated after the metformin treatment of ADSCs.

Met-EVs Ameliorate X-ray-Induced Mitochondrial Dysfunction in Macrophages by Transferring Mitochondria. As the initial step in evaluating the biological effects of Met-EVs, we first incubated 1,1′-dioctadecyl-3,3,3′,3′-tetramethylindocarbocyanine perchlorate dye (Dil, red)-labeled Met-EVs with THP-1 macrophages for 24 h. Using CLSM, Met-EVs were observed to be endocytosed by macrophages (See Methods—Endocytosis of the EVs and Figure S6). We then performed a colocalization experiment between mitochondria-containing Met-EVs (prelabeled with MTDR, red) and endogenous mitochondria (prelabeled with MitoTracker Green FM, MTG, green) in macrophages. The CLSM results showed that mitochondria (red) in Met-EVs were transferred to recipient macrophages 24 h after incubation, and some were fused with the host mitochondrial network (green) (Figure 3A).

Mitochondrial dysfunction and mtDNA mutations following radiation exposure play key roles in chronic oxidative stress. To further verify the therapeutic effect of Met-EVs on radiation combined injury wound healing and the role of mitochondrial transfer during this process, we established X-ray-induced mitochondrial dysfunction models *in vitro*. Macrophages were irradiated with X-rays at doses of 2 and 4 Gy, based on a previous report.[33] After measuring intracellular adenosine 5′-triphosphate (ATP) and ROS levels at 3 and 24 h postirradiation, we found that macrophages were more sensitive to low-dose (2 Gy) irradiation. Eventually, we irradiated the macrophages with X-rays at a dose of 2 Gy to induce mitochondrial dysfunction (Figure S7). Macrophages were treated with a series of concentrations of Met-EVs immediately after X-ray irradiation, and mitochondrial function was assessed by determining ATP levels (Figure S8) and ROS generation in macrophages at 3 and 24 h (see Methods—ATP content assay and ROS content assay). Consistent with previous reports,[33,34] THP-1 macrophages exposed to X-rays showed increased ROS levels, decreased ATP levels, and intracellular mitochondrial dysfunction. Treatment with Met-EVs increased ATP levels and decreased ROS production in a dose-dependent manner, with 1.0×10^8 and 3.0×10^8 particles/mL Met-EVs showing significant effects 3 and 24 h after treatment, respectively (Figure 3B–D). To further demonstrate that Met-EVs ameliorate macrophage mitochondrial dysfunction by transferring active mitochondria, we compared the effects of Met- and Ctrl-EVs on X-ray-induced macrophage mitochondrial dysfunction at a concentration of 10^8 particles/mL (Figure 3B). As shown in Figure 3E–H, compared with unirradiated macrophages (Control group), mitochondrial dysfunction was observed in irradiated macrophages (IR + PBS) 3 and 24 h postirradiation, corroborated by decreased ATP production (Figure 3E), increased ROS content (Figure 3F), and decreased MMP ($\Delta\Psi$m) (see Methods—Cellular MMP assay: JC-1 assay and Figure 3G,H). As expected, Met-EVs were superior in ameliorating mitochondrial dysfunction than Ctrl-EVs in macrophages.

Other cells, including keratinocytes, fibroblasts, and vascular endothelial cells, may also take up mitochondria-containing Met-EVs, resulting in better metabolic function and enhanced wound healing. For example, mitochondrial translocation has been demonstrated to increase MSC migratory capacity[35] and human umbilical vein endothelial cell (HUVEC) angiogenesis.[36] Indeed, we confirmed a better improvement in the MMP of Met-EVs than that of Ctrl-EVs in human epidermal keratinocytes (HaCAT), human foreskin fibroblasts (HFF), and HUVECs, as shown in Figure S9.

https://doi.org/10.1021/acsnano.4c06921
ACS Nano 2024, 18, 26733−26750

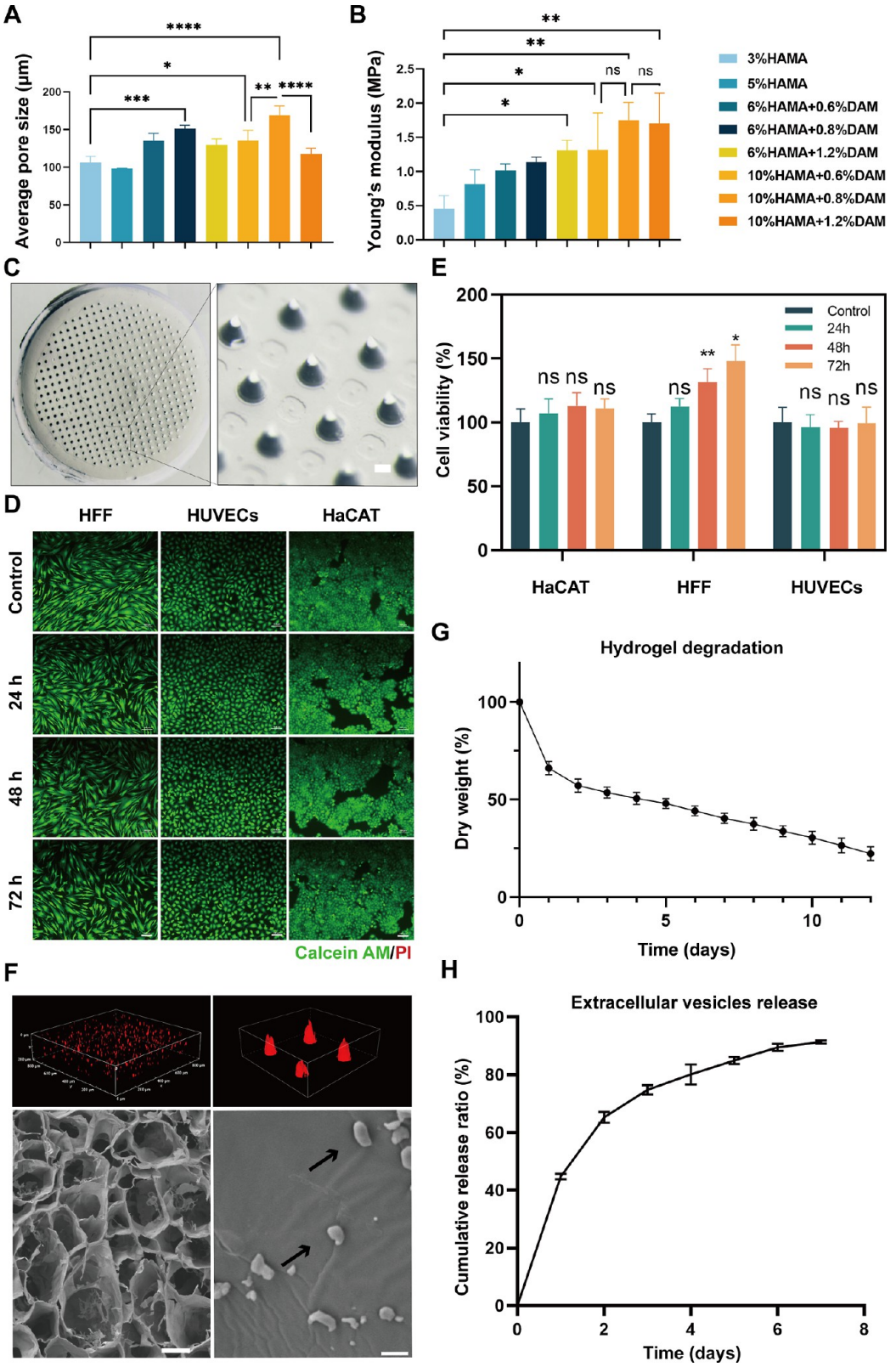

Figure 4. Preparation and characterization of Met-EVs@DAM/HAMA-MNP. (A) Mean pore size of each hydrogel group at different concentration ratios (n = 3). (B) Compression moduli of each group of hydrogels at different concentrations (n = 3). (C) Stereoscopic DAM/HAMA-MNP images. The diameters of MNP tip spacing, height, and base were 700, 500, and 270 μm, respectively. Scale bar, 100 μm. Live and dead cell assays (D) and CCK-8 assays for cell viability (E) of HFF, HUVECs, and HaCAT cells treated with liquid DAM/HAMA hydrogel extracts produced at indicated time points (0, 24-, 48-, 72 h). The cells were labeled with Calcein AM (green) and PI (red) in (D). Scale bars in (D), 100 μm. (F) Top left and right: confocal laser scanning microscopy (CLSM) scanning for 3D reconstruction of the images of MNP loaded with Dil-labeled EVs (red); bottom left and bottom right: scanning electron microscopy (SEM) images of DAM/HAMA-MNPs loaded with EVs, indicated by black arrows. Scale bar, bottom left 100 μm, bottom right 1 μm. (G) *In vitro* degradation curve of the DAM/HAMA hydrogel

https://doi.org/10.1021/acsnano.4c06921
ACS Nano 2024, 18, 26733−26750

Figure 4. continued

($n = 3$). (H) EV release curve of Met-EVs@DAM/HAMA analyzed using the bicinchoninic acid (BCA) assay ($n = 5$). ns, $p > 0.05$, *$p < 0.05$, **$p < 0.01$, ***$p < 0.001$, and ****$p < 0.0001$. Met, metformin; EVs, extracellular vesicles; DAM, decellularized adipose matrix; HAMA, hyaluronic acid methacrylic acid; MNP, microneedle patch; HFF, human foreskin fibroblast; HUVECs, human umbilical vein endothelial cells; HaCAT, human epidermal keratinocytes; CLSM, confocal laser scanning microscopy.

These results suggest that Met-EVs can alleviate mitochondrial dysfunction in cells by transferring active mitochondria and that this regulatory effect is better than that of Ctrl-EVs.

Preparation and Characterization of MNP Loaded with Met-EVs. In the previous study, we showed direct intravenous injection of platelet-derived EVs into irradiated mice increased the number of megakaryocytes and platelet differentiation from hematopoietic stem/progenitor cells in the bone marrow.[37] In the present study, to enable efficient and slow release of Met-EVs into wound tissues, we used human DAM (Figure S10), as we previously reported,[38,39] combined with HAMA to construct an MNP *via* ultraviolet light (UV) curing. To optimize the appropriate scaffold structures for EV loading, we mixed a series of DAM concentrations (w/w: 0.6, 0.8, and 1.2%) with HAMA (w/w: 6 and 10%) hydrogels. After comparing the average pore sizes and compressive moduli of each group of hydrogels (Figure 4A, B), we selected an equal volume ratio of 10% HAMA and 0.8% DAM hydrogels (with a pore size of 168.96 μm and Young's modulus of 1.75 MPa) to prepare the MNP (Figure 4C) after loading with Met-EVs at a final concentration of 3×10^8 particles/mL (see Methods—Preparation of Met-EVs@DAM/HAMA-MNP).

Biocompatibility is a crucial parameter for assessing the quality of biomaterials. To determine the cell viability and the growth of cells cultured in medium containing liquid DAM/HAMA hydrogel extracts, we performed live/dead cell staining and CCK-8 assays, as depicted in Figure 4D, E. The DAM/HAMA hydrogels exhibited good biocompatibility properties *in vitro*. To further assess the biocompatibility of the MNP *in vivo*, we subcutaneously implanted the HAMA, DAM/HAMA, and Met-EVs@DAM/HAMA hydrogels in C57 mice. The periplasmic tissues surrounding the implanted scaffolds were excised 1 week later and subsequently stained for three typical inflammation markers: CD3 (T cells), CD68 (macrophages), and myeloperoxidase (MPO, neutrophils). As shown in Figure S11, none of the three hydrogel groups induced a significant inflammatory response. Finally, we confirmed the presence of Met-EVs in the DAM/HAMA-MNP. Met-EVs were labeled with Dil dye (red) before incorporation into the hydrogels. Three-dimensional (3D) imaging by confocal laser scanning microscopy (CLSM) revealed that the EVs were thoroughly and evenly spread throughout the MNP (Figure 4F, top left and top right). Moreover, SEM revealed that intact Met-EVs were carried by the lyophilized scaffold material (Figure 4F, bottom left and bottom right). These results indicate the successful loading of EVs into the hydrogels. The degradation and sustained-release properties of the hydrogels were measured *in vitro* (see Methods—Degradation properties of DAM/HAMA gels and Assay of EV release from Met-EVs@DAM/HAMA gels), and the curves are shown in Figure 4G, H and Figure S12. The scaffold material degraded slowly, and the EVs were released gradually, with approximately 80% of the EVs being released cumulatively in the first 4 days. These results suggest that Met-EVs@DAM/HAMA-MNP has good biocompatibility and can provide sustained and efficient delivery of EVs to wounded tissues.

We selected DAM/HAMA-MNPs as carriers for the efficient and sustained release of Met-EVs into irradiated wound tissues owing to their several indispensable advantages. (1) MNPs are preferred for enhanced tissue uptake of EVs and EV release, as well as excellent stem cell scaffold.[40] Hydrogel microneedles exhibit better biocompatibility than traditional microneedles. Among these candidates, hyaluronic acid (HA) is a widespread extracellular matrix (ECM) constituent present in almost all human body tissues and plays a vital role in wound healing and tissue regeneration.[41] HA modified by methacrylic anhydride together with UV photocrosslinking was employed to produce hydrogels reminiscent of the primary constituents of natural ECM,[42−44] although HA lacks the naturally occurring peptide portion responsible for adhesion that many ECM proteins possess. Natural DAM hydrogels enhance cell adhesion and facilitate tissue repair owing to the retention of an effective collagen scaffold structure and biofactors, as previously reported.[33,38] Therefore, we combined these (DAM/HAMA-MNP) to construct a better physiological environment to maintain the biological activity of mitochondria-containing EVs. (2) Hydrogel MNPs are more effective vehicles for releasing and transporting EVs. When the Young's modulus of the hydrogel exceeds 1 MPa, the MNP can effectively penetrate wound tissues,[45] while swelling of the hydrogel during water absorption results in larger pore sizes.[46] Our DAM/HAMA hydrogel parameters (pore size of 168.96 μm and Young's modulus of 1.75 MPa) facilitate the release and delivery of EVs into tissue cells,[47,48] as confirmed by our results. (3) Our DAM/HAMA-MNP has superior degradability and absorptive capacity after the painless transdermal delivery of mitochondria, *via* a minimal invasive method with an ideal comfort level,[49] which can result in extraordinary therapeutic effects owing to the dramatically increased contact area between the MNP and the wound.[45]

Met-EVs@DAM/HAMA-MNP Accelerate Wound Healing in Mouse Skin Irradiation Combined Wounds. To confirm the therapeutic efficacy of Met-EVs@DAM/HAMA-MNPs *in vivo*, a dorsal skin radiation-combined wound model was established in C57 mice (see Methods—Met-EVs@DAM/HAMA-MNP-Treated Mice with Irradiated Combined Skin Wounds). As shown in Figure 5A, the model mice were treated with DAM/HAMA-MNP containing Met-EVs at a final concentration of 3×10^8 particles/mL (IR + Met-EVs@DAM/HAMA-MNP), and the total healing rate was compared with that of the other groups: DAM/HAMA-MNP-treated irradiation-combined (IR + DAM/HAMA-MNP), PBS-treated irradiation-combined (IR + PBS), and PBS-treated unirradiated wounds (Without IR). The results revealed that radiation exposure delayed wound healing in mouse skin. However, it is noteworthy that this delayed healing outcome was significantly ameliorated in the Met-EVs@DAM/HAMA-MNP treatment group. Wounds treated with Met-EVs@DAM/HAMA-MNPs healed by postoperative days (POD) 12, which was close to the wound healing time of the Without IR group (POD9). The healing time was significantly faster than that in the IR + DAM/HAMA-MNP (POD14) and IR + PBS groups (wounds that remained unhealed by POD14) (Figure 5B,C).

https://doi.org/10.1021/acsnano.4c06921
ACS Nano 2024, 18, 26733−26750

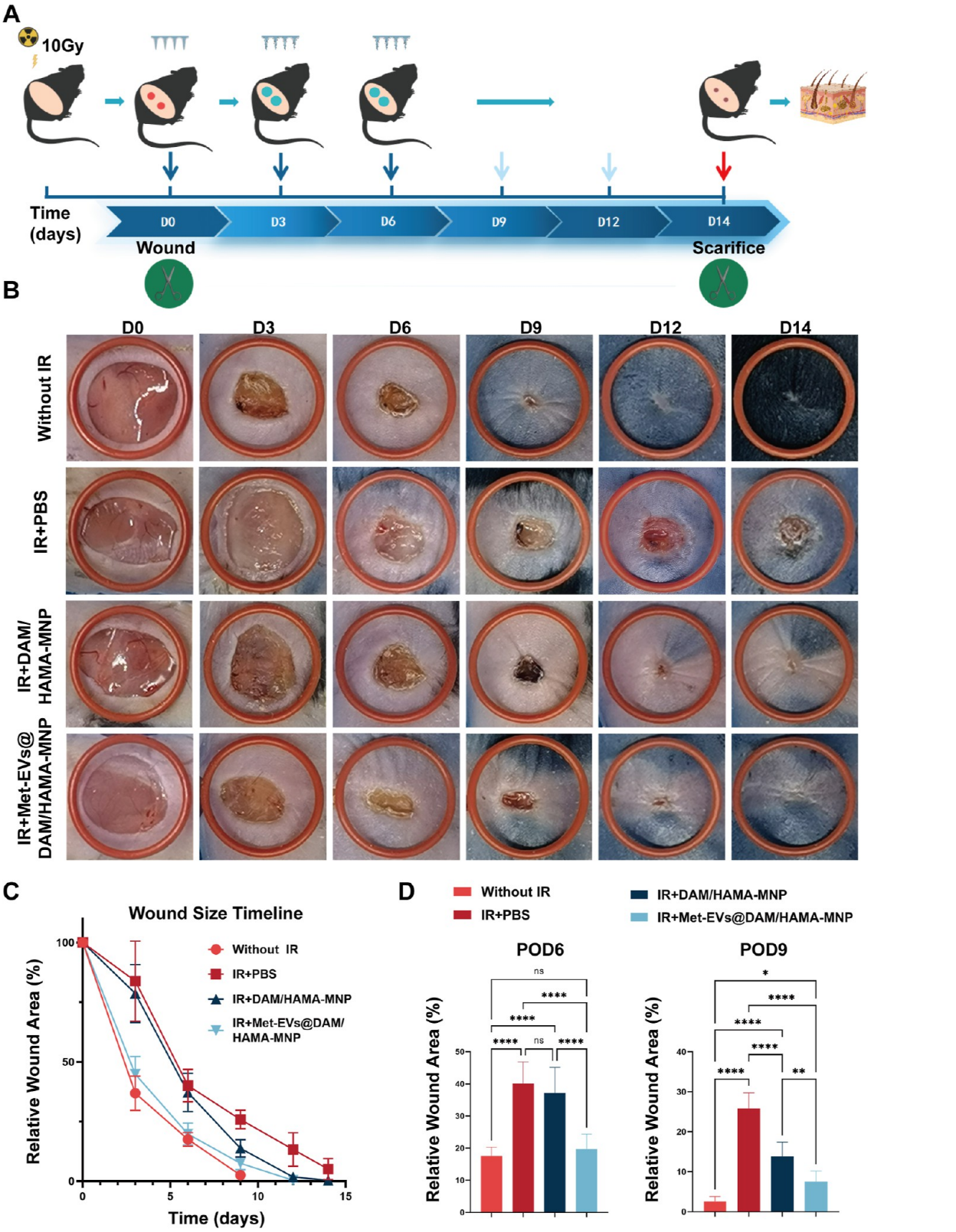

Figure 5. Met-EVs@DAM/HAMA-MNP treatment for radiation combined with skin wounds in mice. (A) Schematic of radiation combined with skin wound model and treatment strategy. (B) Representative graphs of wound healing at each stage in different groups and images of treated wounds on POD 0, 3, 6, 9, 12, and 14. (The red rubber ring has an inner diameter of 14 mm.) (C) Healing curves of the dorsal wounds of mice in each group. The healing curves reflected the relative wound area rate at each stage of the postoperative period (n = 8). (D) Statistical analysis of the relative wound areas in each group on POD6 and 9 (n = 8). ns $p > 0.05$, *$p < 0.05$, **$p < 0.01$, and ****$p < 0.0001$. Met, metformin; EVs, extracellular vesicles; DAM, decellularized adipose matrix; HAMA, hyaluronic acid methacrylic acid; MNP, microneedle patch.

https://doi.org/10.1021/acsnano.4c06921
ACS Nano 2024, 18, 26733−26750

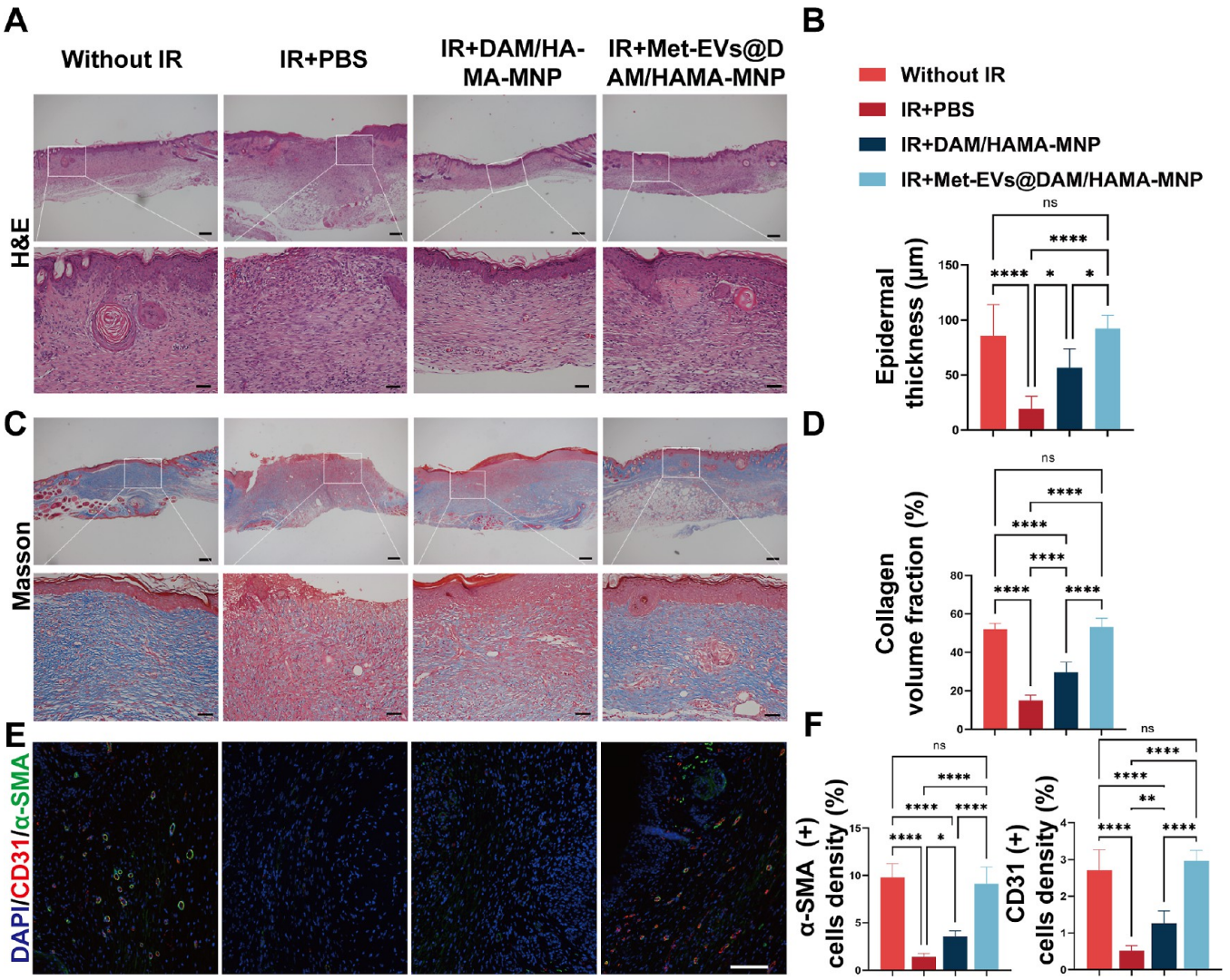

Figure 6. Histological analysis of healed wounds in mice on POD14. (A) Representative images of H&E staining of wound tissues and comparison of wound tissues epithelial thickness (B) on POD14 between each group (n = 6). (C) Masson's trichrome staining on POD14 showed that the IR + PBS group still had a wound with no epidermal overlying tissue and significantly less collagen deposition than those in the other groups. (D) Comparison of collagen deposition fraction on POD14 between each group (n = 6). (E,F) Immunofluorescence staining of wound tissue sections on POD14 by labeling CD31 (red) and α-smooth muscle actin (α-SMA) (green) and comparing the expression levels of CD31 and α-SMA in each group (n = 6). Scale bars: (A) and (C), top, 200 μm, bottom, 50 μm; (E), 100 μm. ns $p > 0.05$, *$p < 0.05$, **$p < 0.01$, and ****$p < 0.0001$. POD, postoperative day; H&E, hematoxylin and eosin; IR, irradiation; PBS, phosphate-buffered saline; α-SMA, α-smooth muscle actin.

Next, we measured the proportion of the remaining wound area in each group of mice on POD6 and 9. As shown in Figure 5D, on POD6, the remaining wound area in the IR + Met-EVs@DAM/HAMA-MNP group (19.75%) was significantly smaller than that in the IR + DAM/HAMA-MNP (37.18%, $p < 0.0001$) and IR + PBS groups (40.07%, $p < 0.0001$), while no significant difference compared to the Without IR group was observed ($p > 0.05$). On POD9, the IR + Met-EVs@DAM/HAMA-MNP group exhibited a significantly smaller percentage of remaining wound area (7.53%) than those of the IR + DAM/HAMA (13.77%, $p < 0.001$) and IR + PBS groups (25.84%, $p < 0.0001$), although it was significantly higher than that of the Without IR group (2.57%, $p < 0.05$).

Next, histopathological analysis of the wounds and surrounding tissues on POD14 was performed using hematoxylin and eosin (H&E) and Masson's trichrome staining. H&E staining demonstrated that the Met-EVs@DAM/HAMA-MNP group had a significantly thicker epithelium (mean = 92.14 μm) compared with that of the IR + DAM/HAMA (mean = 56.44 μm, $p < 0.05$) and IR + PBS groups (mean = 19.15 μm, $p < 0.0001$). Notably, the IR + Met-EVs@DAM/HAMA-MNP group was restored to a level comparable to that of the unirradiated skin group (85.45 μm, $p < 0.0001$) (Figure 6A, B). This suggests that IR + Met-EVs@DAM/HAMA-MNP treatment promoted skin wound healing following radiation injury in mice. The assessment of wound tissue collagen deposition in each group by analyzing the type I collagen volume fraction using Masson's trichrome staining was consistent with the H&E results. The IR + Met-EVs@DAM/HAMA-MNP group showed significantly higher collagen deposition (48.15%) than that in the IR + DAM/HAMA (30.23%, $p < 0.0001$) and IR + PBS (14.78%, $p < 0.0001$) groups. No significant difference was observed when compared with the Without IR group (53.02%, $p > 0.05$) (Figure 6C,D).

https://doi.org/10.1021/acsnano.4c06921
ACS Nano 2024, 18, 26733−26750

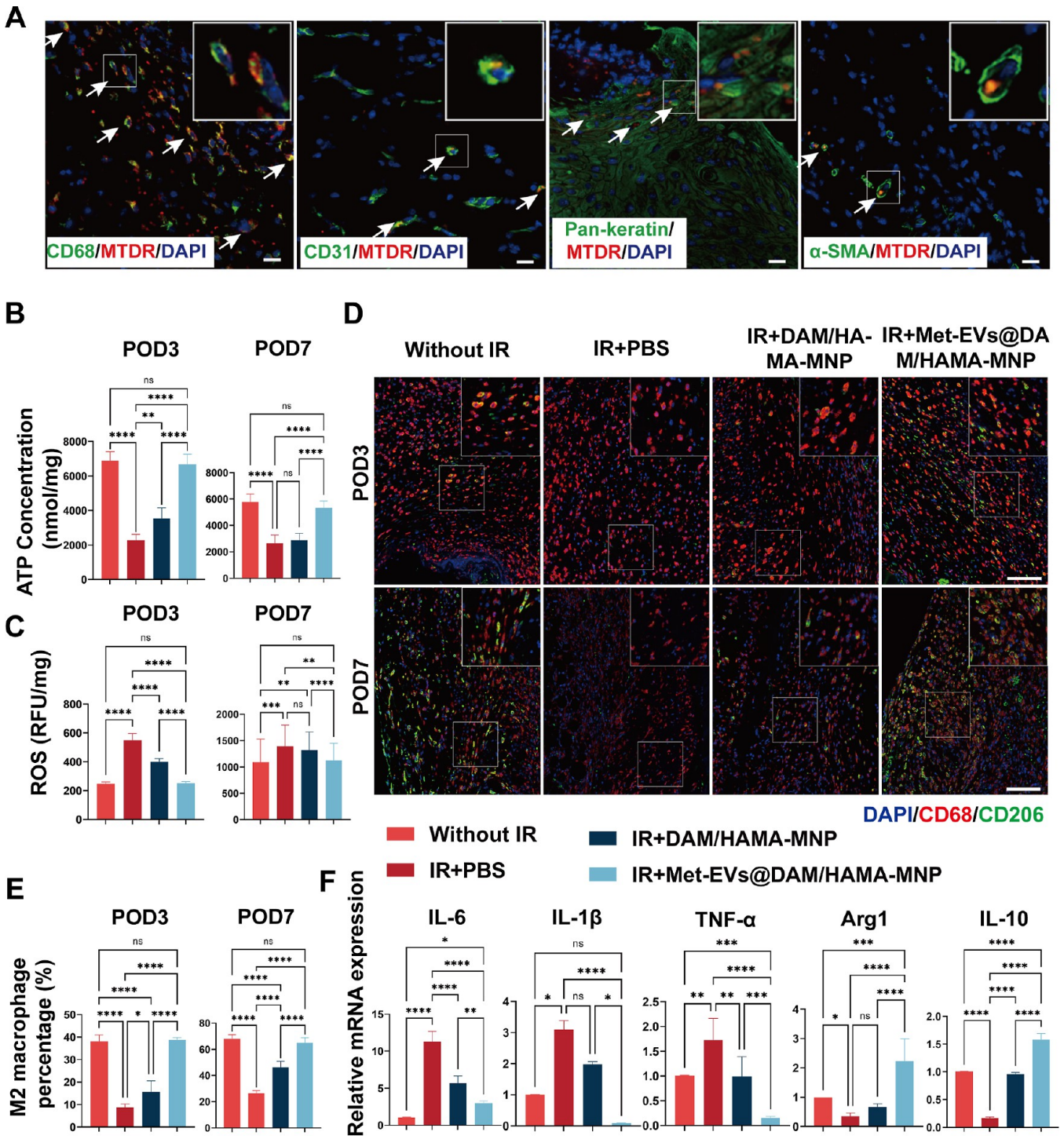

Figure 7. Histological analysis of healed wounds in mice on POD3 and 7. (A) Met-EVs containing MTDR (red)-labeled mitochondria were delivered to the wound, and 3 days later, the tissue was excised and immunofluorescently stained to observe the delivery of mitochondria by Met-EVs to macrophages (CD68, green), vascular endothelial cells (CD31, green), epithelial cells (Pan-keratin, green), and myofibroblasts (α-SMA, green) under CLSM. MTDR-labeled mitochondria (indicated by white arrows) were captured in the wound tissues. Scale bar, 50 μm. (B) ATP content of wound tissues was measured on POD3 and 7 ($n = 6$). (C) ROS levels in wound tissues were measured on POD3 and 7 ($n = 6$). (D) Representative images of the wound tissue stained with CD68 (red) and CD206 (green) on POD3 and 7. Scale bar, 100 μm. (E) Percentage of M2-subtype macrophages (cell number ratio of $CD206^+$ cells to $CD68^+$ cells) in wound tissues on POD3 and 7 ($n = 4–6$). (F) Relative mRNA expression of IL-6, IL-1β, TNF-α, arginase 1 (Arg1), and IL-10 were examined in the wound tissues on POD7 ($n = 4–6$). ns $p > 0.05$, *$p < 0.05$, **$p < 0.01$, ***$p < 0.001$, and ****$p < 0.0001$. POD, postoperative day; Met, metformin; EVs, extracellular vesicles; MTDR, MitoTracker Deep Red; α-SMA, alpha-smooth muscle actin; CLSM, confocal laser scanning microscopy; ROS, reactive oxygen species; IL, interleukin; TNF-α, tumor necrosis factor-α.

Immunofluorescence staining of CD31 (red) and α-SMA (green) was also performed and analyzed in wound tissues on POD14 (Figure 6E, F). The results indicated significant upregulation of CD31 and α-SMA expression in the IR + Met-

https://doi.org/10.1021/acsnano.4c06921
ACS Nano 2024, 18, 26733−26750

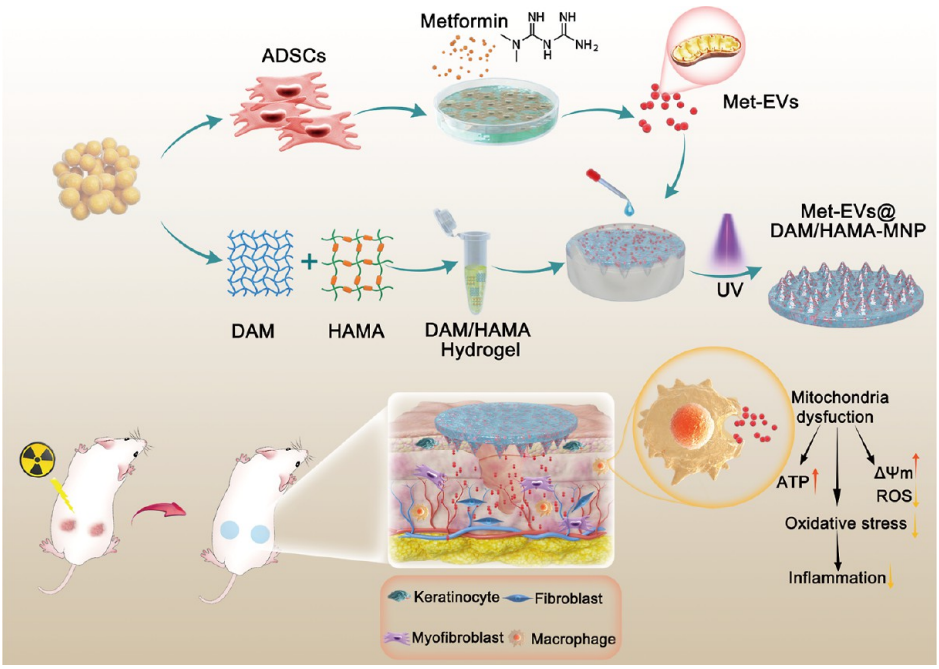

Figure 8. Schematic illustration of the fabrication of Met-EVs@DAM/HAMA-MNP and skin wound treatment in a mice model. Met-EVs@DAM/HAMA-MNPs can continuously and effectively deliver EVs containing active mitochondria to irradiated wound tissues to improve mitochondrial dysfunction by increasing ATP production, decreasing ROS content and oxidative stress pressure, and promoting macrophage polarization from the pro-inflammatory M1-subtype toward the M2-subtype with anti-inflammatory and wound healing functions in skin wound tissues.

EVs@DAM/HAMA-MNP group compared with that in the IR + DAM/HAMA-MNP ($p < 0.0001$) and IR + PBS groups ($p < 0.0001$). No significant difference was observed between the IR + Met-EVs@DAM/HAMA-MNP and Without IR groups ($p > 0.05$).

These results suggest that radiation leads to delayed healing of skin wounds and that treatment with Met-EVs@DAM/HAMA-MNPs reduces this negative effect and facilitates wound healing.

Met-EVs@DAM/HAMA-MNP Improves X-ray-Induced Metabolic Disorders in Wound Tissues. To illustrate the capacity of Met-EVs@DAM/HAMA-MNPs to transport active mitochondria to wounded tissues, we incorporated MTDR-labeled Met-EVs (red) into DAM/HAMA-MNPs to treat the dorsal skin wounds of C57 mice. Active mitochondria delivered by Met-EVs were observed in the wound tissues 3 days post-treatment, as determined by immunofluorescence staining (Figure 7A). The results showed that labeled mitochondria were transferred to macrophages (CD68, green), vascular endothelial cells (CD31, green), epithelial cells (Pan-keratin, green), and myofibroblasts (α-SMA, green) in the wound tissue, consistent with our *in vitro* results (Figure S9).

Moreover, to determine whether Met-EVs@DAM/HAMA-MNPs could ameliorate metabolic disorders in wound tissues, we examined the ATP and ROS content within the wound tissues (Figure 7B, C). The results indicated that the ATP concentration in the wound tissues of the IR + Met-EVs@DAM/HAMA-MNP group was significantly higher than that of the IR + DAM/HAMA-MNP and IR + PBS groups on both POD3 and 7 but did not significantly differ from that in the Without IR group (Figure 7B). Accordingly, the ROS content in the wound tissues treated with Met-EVs@DAM/HAMA-MNP was lower than that in the IR + DAM/HAMA-MNP and IR + PBS groups but did not significantly differ from that in the Without IR group (Figure 7C).

To investigate whether Met-EVs@DAM/HAMA-MNP treatment regulates macrophage polarization, we stained excised tissues with the macrophage surface marker CD68 (red) and the M2 subtype macrophage surface marker CD206 (green) on POD3 and 7. The percentage of M2 macrophages in the wound area was significantly higher in the IR + Met-EVs@DAM/HAMA-MNP group than that in the IR + DAM/HAMA-MNP and IR + PBS groups, while no significant difference from that of Without IR was observed (Figure 7D, E). These results indicated that Met-EVs@DAM/HAMA-MNPs promoted macrophage differentiation from the M1 to M2 subtype within wound tissues. Consistently, qPCR results showed that the expression levels of pro-inflammatory factors including interleukin-6 (IL-6), IL-1β, and tumor necrosis factor-alpha (TNF-α) in the Met-EVs@DAM/HAMA-MNP group were significantly lower than those in the IR + DAM/HAMA-MNP and IR + PBS groups; in contrast, the expression levels of anti-inflammatory factors including Arg1 and IL-10 were significantly higher than those in the IR + DAM/HAMA-MNP and IR + PBS groups on POD7 (Figure 7F).

In vivo, radiation exposure leads to the inflammatory cell infiltrations, which become important sources of ROS and nitric oxide.[50] An imbalance in macrophage metabolism leads to impaired tissue repair and wound healing.[51,52] Our animal experiments showed that Met-EVs@DAM/HAMA-MNPs effectively transported ADSC-derived mitochondria into wound tissues. Treatment with Met-EVs@DAM/HAMA-MNPs resulted in enhanced ATP production, reduced ROS levels, and promoted the polarization of macrophage from the pro-inflammatory M1-subtype toward the M2-subtype with anti-inflammatory and wound-healing functions in skin wound tissues.

We acknowledge the limitations of this study. First, EVs were prepared by differential centrifugation at 2000 × *g* to remove

https://doi.org/10.1021/acsnano.4c06921
ACS Nano 2024, 18, 26733−26750

apoptotic bodies and cellular debris, followed by centrifugation at 20,000 × *g* to obtain larger EVs; therefore, we could not completely exclude EVs with a size < 300 nm. Second, we only examined the active mitochondrial components of the vesicles that may alleviate mitochondrial dysfunction. However, the presence of other RNAs or mtDNA fragments present in the vesicles that may also alleviate cellular metabolic dysfunction cannot be ignored. The use of mitochondria-containing EVs has certain drawbacks, such as low strength and restricted drug doses. Nonetheless, we observed that the mitochondria-containing EVs, loaded and delivered by hydrogel-forming MNPs, has good therapeutic effects on chronic wound healing. We believe that, with advancements in the hydrogel MNP preparation techniques and deep understanding of how to regulate mitochondria package and transfer with EVs, better therapeutic effects can be achieved in future applications.

CONCLUSIONS

Together, we successfully constructed a DAM/HAMA-MNP loaded with mitochondria-containing EVs that effectively treated skin wounds combined with radiation injuries by promoting mitochondrial transfer. These Met-EVs contained active mitochondria capable of ameliorating mitochondrial dysfunction and facilitating macrophage polarization toward the M2 phenotype. The efficacy of Met-EVs@DAM/HAMA-MNPs in repairing chronic wounds was proven *in vivo* and holds great potential for future clinical wound care (Figure 8).

METHODS

Patients and Ethics Approval. ADSCs were obtained from discarded adipose tissue after abdominal and thigh liposuction in the Plastic Surgery Department of the First Medical Center of the General Hospital of the Chinese People's Liberation Army (PLA). All patients provided the informed consent. The inclusion criteria were the absence of systemic diseases, and current or recent drug treatment. Exclusion criteria were patients over the age of 45 or those who refused to provide a specimen. The Ethics Committee of the Chinese PLA General Hospital approved the study protocol (S2023-207-01).

ADSC Isolation, Culture, and Characterization. ADSCs were prepared and cultured as we previously described.[53] Human adipose tissue was digested with type I collagenase, and ADSCs from passage three were used for EV isolation. ADSCs were cultured in human ADSC medium (Cyagen, Santa Clara, CA, USA). To determine ADSC surface marker expression, ADSCs were incubated with fluorescence-labeled antibodies, including CD29-APC, CD73-APC, CD105-PE, CD166-PE, CD14-APC, CD34-APC, and CD45-APC (BD Biosciences, Franklin Lakes, NJ, USA) and CD31-APC, CD38-APC, and CD90-PE-cy7 (eBioscience, Santa Clara, CA, USA), and analyzed by flow cytometry (Luminex Guava easyCyte; Luminex Corporation, Austin, TX, USA). The trilineage differentiation of ADSCs was performed using the appropriate induction media (human adipose-derived MSC adipogenic differentiation medium, human adipose-derived MSC osteogenic differentiation medium, and human adipose-derived MSC chondrogenic differentiation medium; Cyagen), analyzed by Alizarin Red, Oil Red O, and Alcian Blue staining, according to the manufacturer's instructions.

Isolation and Characterization of EVs. For Met-EV isolation, ADSC medium containing 75 μM metformin was replaced and induced for 48 h after cultivating ADSCs at passage 3 to approximately 60% confluence. After two washes with PBS, ADSC medium containing 10% exosome-free fetal bovine serum (FBS, Cagen) was added. After 48 h of incubation, the medium was collected, and the supernatant was collected by centrifugation at 300 × *g* for 5 min to remove dead cells. Subsequently, the supernatant was centrifuged at 2000 × *g* for 10 min to remove apoptotic bodies and cellular debris, followed by two rounds of centrifugation at 20,000 × *g* for 60 min, after which the pellet was resuspended in PBS. Ctrl-EVs were cultured in ADSC medium without metformin. All EVs extraction steps were performed at 4 °C to ensure EVs activity.

The size distribution and concentration of EVs were analyzed by NTA using a ZetaView Particle Tracker (Particle Metrix, Inning am Ammersee, Germany). EV morphology was observed using TEM (HT7800; Hitachi High-Tech Corporation, Tokyo, Japan). EV marker levels (CD9 and TSG101) and the mitochondrial outer membrane protein Tom20 were analyzed using a capillary immunoassay (Protein Simple; Biotechne, Minneapolis, MN, USA).

Flow Cytometric Analysis of EVs. Mitochondria were labeled before changing to the exosome-free FBS-containing medium, and residual FBS was removed by washing with PBS before staining. Mitochondria in isolated EVs were derived from ADSCs prestained with 200 nM MTDR (Thermo Fisher Scientific, Waltham, MA, USA) in 10 mL of standard serum-free medium and incubated for 45 min at 37 °C in the dark. After five washes with PBS, the exosome-depleted medium was changed. The supernatant was harvested for EV extraction after 48 h. Thereafter, the EVs were resuspended in 100 μL PBS, stained with propidium iodide (necrosis), Annexin V-BV421 (apoptosis), and antihuman CD44-PE-Cy7 for 40 min at 4 °C in the dark, washed with 1 mL PBS, and centrifuged at 20,000 × *g* for 60 min at 4 °C. Next, the pellet was collected and resuspended in 300 μL PBS. Standard-sized 200-, 500-, and 1000 nm beads (Thermo Fisher Scientific) were used as a reference for comparison with EVs in the forward vs side scatter (FSC vs SSC) plots. The gating strategy was as follows: using standard beads as a reference, EVs were gated by FSC and SSC to select EVs of 200−1000 nm size, after which events negative for propidium iodide staining (necrosis) were gated; Annexin V staining (apoptosis) was excluded. Based on previous report,[17] the final gate was used to determine the proportion of EVs expressing CD44 and containing mitochondria (MTDR).

KEGG and GO Enrichment Analyses of Differential Proteins between Met- and Ctrl-EVs. Two sets of EV protein samples were separated by chromatography and analyzed by mass spectrometry (MS) using an Orbitrap Exploris 480 mass spectrometer. MS data were analyzed using MaxQuant software version 1.6.17.0. The protein sequence database was: uniprot_homo_20221024_20402_9606_s-wiss_prot. The GO and KEGG databases used in this project are versioned as go.obo (2019.07.01) and KO−INFO-END.txt (2022.11.05), respectively. Enrichment analysis algorithms for GO and KEGG annotations are consistent. Fisher's exact test was used to compare the distribution of each GO term or KEGG pathway in the target and total protein set. The significance level of GO term or KEGG pathway enriched was subsequently assessed. The WoLF PSORT[54] was used to predict the subcellular localization of proteins. The MS proteomics data have been deposited to the ProteomeXchange Consortium (https://proteomecentral.proteomexchange.org) *via* the iProX partner repository[55,56] with the data set identifier PXD048824.

Preparation of Met-EVs@DAM/HAMA-MNP. To prepare the DAM hydrogel, human adipose tissues discarded from healthy patients after liposuction were decellularized. The Ethics Committee of the Chinese PLA General Hospital approved the study protocol (2019-X15−02). Briefly, adipose tissues were first subjected to three freeze−thaw cycles, digested with trypsin (Gibco, Grand Island, NY, USA) and nuclease (HaiGene, Harbin, China), extracted with isopropyl alcohol, and finally lyophilized to produce DAM. The DAM was ground into a powder in liquid nitrogen. Subsequently, the DAM digest was prepared by treatment with a pepsin solution (1 mg/mL; Sigma-Aldrich, St. Louis, MO, USA) containing 0.01 mol/L HCl for 48−72 h. The pH was adjusted to approximately 7.4 for DAM hydrogels by adding 10× α-MEM (Gibco) and an appropriate amount of 1 mol/L NaOH at 4 °C. The hydrogel concentrations were 0.6, 0.8, and 1.2% (w/w). The prepared DAM was characterized by H&E, Masson's trichrome, Oil Red O, and immunofluorescence staining and SEM (Hitachi Regulus 8100; Hitachi High-Tech Corporation).

HAMA (150 kDa) was purchased from Engineering for Life Sciences (EFL, Suzhou, China) and mixed with 0.25% (w/w) lithium acylphosphate photoinitiator to prepare 3, 5, 6, and 10% (w/w) HAMA pregels. The DAM hydrogel was then mixed with the HAMA

https://doi.org/10.1021/acsnano.4c06921
ACS Nano 2024, 18, 26733−26750

pregel in equal volumes, and the cross-link was exposed to 405 nm visible light for 30 s to cure a cylindrical gel 13 mm in diameter and 6 mm in height. The compressive moduli of the gels with different concentration ratios were measured using an HZ-1004 Material Testing System (Dongguan Lixian Instrument Scientific Co., Ltd., Dongguan, China). Simultaneously, the gels were freeze-dried, and the pore sizes of the gels with different ratios were observed and compared using SEM after brittle fracture.

To prepare Met-EVs@DAM/HAMA-MNPs, after injecting 0.8% DAM and 10% HAMA pregel into the microneedle mold (EFL-MMN-500, circle, diameter 17.5 mm), the mixture was centrifuged at 1500 × *g* for 3 min to remove bubbles and subjected to cross-linking under visible light at 405 nm for 30 s to cure the DAM/HAMA-MNPs. Met-EVs@DAM/HAMA-MNPs were prepared by adding PBS-resuspended Met-EVs to DAM/HAMA before addition to a microneedle mold. The pregel was mixed, and the final concentration of Met-EVs was 3×10^8 particles/mL.

DAM/HAMA Hydrogel Biocompatibility Assay. HUVECs, HaCATs, and HFFs were used to evaluate DAM/HAMA hydrogel biocompatibility *in vitro*.[46] DAM/HAMA hydrogels were immersed in complete medium containing Dulbecco's modified Eagle's medium (DMEM, high-glucose) with 10% FBS for different periods (0, 24, 48, and 72 h). The extracted fluid was then collected for biocompatibility testing. The LIVE/DEAD assay (Beyotime Biotechnology, Shanghai, China) was used to assess cell activity, while cell viability was estimated using a CCK-8 assay (Dojindo Laboratories, Japan). Approximately 8×10^3 HaCATs, 4×10^3 HUVECs, and 3.2×10^3 HFFs were seeded in 96-well plates with 100 μL extract liquid per well for 24 h, with six parallel controls for each group. Next, 100 μL of working reagent was added to each well and incubated at 37 °C for 1 h before detection.

For the *in vivo* biocompatibility assay, female C57BL/6J (6−8 weeks old; Vital River Laboratory Animal Technology, Beijing, China) were used. A 1 cm skin incision was made in the middle of the backs of the mice, and the cavities were peeled off at the subcutaneous level. Thereafter, HAMA, DAM/HAMA, and Met-EVs@DAM/HAMA hydrogels ($n = 6$) were implanted subcutaneously into the backs under sterile conditions. Mice were sacrificed 1 week after surgery, and the samples were processed for histological analysis.

Endocytosis of the EVs. THP-1 cells (Procell CL-0233; Procell Life Science & Technology Co., Ltd., Wuhan, China) were cultured in RPMI-1640 medium containing 10% FBS, 1% penicillin/streptomycin and 0.05 mM β-mercaptoethanol and incubated in a 37 °C 5% CO_2 incubator. Cells were grown at a density of 2×10^5 cells/mL. To induce THP-1 cell differentiation into macrophages, THP-1 cells were incubated with 100 nM phorbol 12-myristate 13-acetate (PMA) for 48 h before the experiment.

To well-label EVs and trace their movement under a CLSM (ZEISS LSM 980; ZEISS, Oberkochen, Germany), Dil (red; Beyotime Biotechnology) was used. First, an equal volume of the working solution containing 10 μM Dil was added to the EV suspension, and then the mixture was incubated at 37 °C for 15 min in the dark. Afterward, we diluted the mixture by adding 5× PBS, after which the Dil-labeled EVs were centrifuged at 20,000 × *g* for 60 min and resuspended in PBS. Subsequently, the labeled EVs were incubated with PMA-induced THP-1 macrophages for 24 h. Next, the cells were fixed with 4% paraformaldehyde and stained with 4′,6-diamidino-2-phenylindole (DAPI; Thermo Fisher Scientific) and a microfilament green fluorescent probe (Beyotime Biotechnology) for 20 min. The cells were observed using CLSM to monitor the endocytosis of EVs by macrophages.

Degradation Properties of DAM/HAMA Gels. The pregel (0.8% DAM +10% HAMA) (200 μL) was exposed to light, dried in an oven at 75 °C for 4 h, and weighed ($W0$). Subsequently, the gel was immersed in PBS buffer containing 100 U/mL of hyaluronidase (EFL) and 0.1% type I collagenase (Sigma-Aldrich) and placed in a shaker (150 rpm, 37 °C) for digestion for 24 h. Next, after the PBS solution discarded, the gels were dried in an oven at 75 °C for 4 h, after which they were weighed ($W1$); the weight of the gel residue (Wx) was continuously monitored during the experiment. The dry weight ratio (ΔW %) was defined as $\Delta W\% = Wx/W0 \times 100\%$.

Assay of EV Release from Met-EVs@DAM/HAMA Gels. Dil-labeled EVs were mixed with the DAM/HAMA pregel and cured using light. Thereafter, CLSM was used to image the samples, which were subsequently reconstructed into 3D images to observe the loading of EVs onto the DAM/HAMA hydrogel.

After measuring the concentration of Met-EVs using the BCA method, they were mixed with the DAM/HAMA pregel to achieve a final concentration of EVs of 500 μg/mL. Subsequently, 100 μL of the pregel, photopolymerized into a cylindrical shape, was aspirated into each sample well of a 24-well plate. Each well was immersed in 800 μL of PBS at 37 °C. The DAM/HAMA gel without EVs served as the control group. The 400 μL of PBS solution in each well was replaced daily, with the replaced solution used for BCA protein concentration detection for a period of 7 days. Cumulative EV release (Q) was calculated as follows

$$Q(\%) = \frac{V\sum_1^{n-1}(C_{it} - C_{i\mathrm{ctrl}}) + V_0(C_{nt} - C_{n\mathrm{ctrl}})}{M} \times 100\%$$

where V is the liquid volume per PBS change (400 μL), V_0 indicates each well plate containing a total of liquid (800 μL), C_{it} is the protein concentration of the ith experimental group, $C_{i\mathrm{ctrl}}$ is the concentration of the ith protein measured in the control group, C_{nt} is the concentration of the nth protein measured in the experimental group, $C_{n\mathrm{ctrl}}$ is the concentration of the nth protein measured in the control group, and M is the total EV protein loaded at 50 μg.

ATP Content Assay. For cell sample collection, cells were washed twice with 1 mL of PBS and lysed by 200 μL of lysis solution into each well of a 6-well plate. After lysis, the cells were centrifuged at 12,000 × *g* for 5 min at 4 °C, after which the supernatant was collected for testing. For skin tissue collection, fresh tissue samples were rinsed with PBS and weighed. Thereafter, 200 μL of lysate for every 20 mg of tissue was added and homogenized well using a tissue grinder (Servicebio, Wuhan, China) at −20 °C. After the tissue was lysed, it was centrifuged at 12,000 × *g* for 5 min at 4 °C, and the resulting supernatant was obtained for further analysis. Next, 100 μL of an ATP assay working solution (Beyotime Biotechnology) was added to a 96-well plate, and a control group was established by adding the working solution only. After 3−5 min at 25 °C, 20 μL of the sample was quickly mixed using a pipet gun and added to the assay wells. Subsequently, relative light unit values were determined at intervals of at least 2 s using a multifunctional enzyme reader (Spectramax M2e; Molecular Devices, San Jose, CA, USA). The ATP content in each group was calculated using a standard curve.

For the tissue ATP assay, a separate supernatant of the homogenate was used, and the protein content was assessed using the BCA method. The ATP concentration was then converted into nmol/mg protein units for comparative purposes. All the procedures were conducted on ice.

ROS Content Assay. To determine intracellular ROS content, the cells were rinsed twice with PBS, digested with trypsin, and centrifuged at 150 × *g* for 4 min. The cells in the assay group were resuspended in 100 μL of CellRox working solution (Thermo Fisher Scientific) containing 5 μM of CellRox, while the cells in the blank group were resuspended in 100 μL of PBS. Both groups were incubated in the darkness for 30 min at 37 °C, followed by dilution with 1 mL PBS and cell centrifugation. The cells were then resuspended in 300 μL PBS, and the mean green fluorescence intensity was analyzed using flow cytometry.

For skin tissue ROS determination, all procedures were performed on ice. Briefly, fresh tissue samples were weighed, after which 1 mL of homogenization buffer per 50 mg of tissue was added, and the mixture was ground well using a tissue grinder at −20 °C. Next, the homogenate was centrifuged at 1000 × *g* for 3 min at 4 °C, then, 200 μL of the homogenized supernatant and 2 μL of dihydroethidium probe (Tissue ROS Test Kit; BIO-LAB, Beijing, China) were added to a 96-well plate and mixed well by blowing up the supernatant with a pipet. The plate was then incubated at 37 °C in the darkness for 30 min. Next, the fluorescence intensity of the sample was determined using a multifunctional enzyme reader (Spectramax M2e, Molecular Devices).

https://doi.org/10.1021/acsnano.4c06921
ACS Nano 2024, 18, 26733−26750

In addition, another homogenate was used to quantify the protein levels. The resulting relative fluorescence unit/mg protein value (RFU/mg) indicated the levels of tissue ROS.

Cellular MMP Assay: JC-1 Assay. After washed with PBS, 1 mL of medium was added to the cells. Subsequently, 1 mL of JC-1 staining working solution (Beyotime Biotechnology) was added and mixed thoroughly. After a 20-min incubation at 37 °C in the cell incubator, the supernatant was removed, and the cells were washed twice with JC-1 staining buffer. Finally, 2 mL of cell culture solution was added, and observation and imaging were conducted using CLSM.

Met-EVs@DAM/HAMA-MNP-Treated Mice with Irradiated Combined Skin Wounds. Female mice heal skin wounds faster than males, and the mixed allocation of males and females may affect the healing time of wounds in each group;[57] while male mice are more aggressive and are prone to bite wounds when kept in the same cage.[58] Therefore, female mice were selected for *in vivo* experiments in this study. Forty-eight female C57BL/6J mice aged 6−8 weeks were divided into four groups. Thirty-six of them were randomly assigned to study irradiated wound healing and were divided equally into three treatment groups: DAM/HAMA-MNPs, Met-EVs@DAM/HAMA-MNPs, and PBS-treated controls. The skin was shaved and depilated before X-ray irradiation. Lead shielding was used to safeguard all tissues, excluding the dorsal skin. An overall exposure of 10 Gy was administered to the dorsal skin using an X-ray machine (RS2000; Rad Source Technologies, Buford, GA, USA). Full skin wounds were symmetrically created on the backs of mice irradiated with X-rays using a 10 mm skin perforator 3 days after irradiation, which was considered day 0 of the treatment. An additional 12 mice were used for regular nonirradiated skin wound treatment. The wounds were changed every 3 days until they healed. The wounds were subjected to various therapeutic treatments at POD0, 3, and 6. Tissue metabolism studies were conducted on wound tissues collected on POD3 and 7. Pathological section analysis was performed on wound tissues collected on POD14. Exclusion criteria were the death of mice throughout the experiment, or aggravation or splitting of wounds caused by mouse bites at the wound sites. All animal protocols were approved by the Institutional Animal Care and Use Committee and complied with the guidelines of the Beijing Medical Experimental Animal Care Commission (IACUC-DWZX-2023−525).

Real-Time Quantitative PCR Analysis. Total RNA was extracted using Trizol reagent (Invitrogen, Carlsbad, CA, USA). Subsequently, cDNA synthesis and qPCR were conducted using ReverTra Ace qPCR RT Master Mix (TOYOBO, Shanghai, China) and SYBR Green Real-time PCR Master Mix (TOYOBO), respectively. PCR primer sequences are listed in Table S3. Gene expression was quantified using the delta−delta Ct method.[59] All gene expressions were normalized to mouse GAPDH.

Statistical Analysis. All data are presented as mean ± standard deviation. Statistical analyses were performed using GraphPad Prism 9.0 (GraphPad Software, San Diego, CA, USA). Two-group comparisons were conducted using a paired *t*-test, and multiple-group comparisons were performed using one-way ANOVA (Tukey's posthoc test). Statistical significance was considered at $p < 0.05$: *$p < 0.05$, **$p < 0.01$, ***$p < 0.001$, and ****$p < 0.0001$.

ASSOCIATED CONTENT

Data Availability Statement

The data that support the findings of this study are available from the corresponding author upon reasonable request.

Supporting Information

The Supporting Information is available free of charge at https://pubs.acs.org/doi/10.1021/acsnano.4c06921.

Figure S1 Identification of ADSCs; Figure S2 Dose−response curve of ADSCs treated with metformin or pioglitazone; Figure S3 Relative MTDR expression in ADSCs treated with a series of metformin and pioglitazone concentrations; Figure S4 Gating for flow cytometry (FCM) analysis of active mitochondrial in ADSC-derived EVs; Figure S5 Proteomic analysis of differential proteins between Met- and Ctrl-EVs; Figure S6 Macrophage endocytosis of EVs; Figure S7 Comparison of changes in ATP and ROS after X-ray irradiation of macrophages at 2 or 4 Gy; Figure S8 Standard curve for ATP assay; Figure S9 Met-EVs ameliorate X-ray-induced mitochondrial dysfunction in HaCAT, HFF, and HUVECs; Figure S10 Preparation and characterization of DAM hydrogel; Figure S11 Immunofluorescence staining of infiltrating inflammatory cells in tissue surrounding subcutaneous implants; Figure S12 Standard curve for BCA protein assay. Table S1 Kits and reagents used in the study; Table S2 Antibodies used in the study; Table S3 Primers used for PCR and RT-qPCR in the study (PDF)

AUTHOR INFORMATION

Corresponding Authors

Jun-Nian Zhou − *Beijing Institute of Radiation Medicine, Beijing 100850, China;* orcid.org/0000-0002-7782-234X; Email: zhoujunnian@bmi.ac.cn

Yan Han − *School of Medicine, Nankai University, Tianjin 300071, China; Department of Plastic and Reconstructive Surgery, The First Medical Centre, Chinese PLA General Hospital, Beijing 100853, China;* orcid.org/0000-0002-6810-2957; Email: 13720086335@163.com

Wen Yue − *Beijing Institute of Radiation Medicine, Beijing 100850, China;* orcid.org/0000-0002-3935-360X; Email: yuewen@bmi.ac.cn

Authors

Wen-De Yao − *School of Medicine, Nankai University, Tianjin 300071, China; Department of Plastic and Reconstructive Surgery, The First Medical Centre, Chinese PLA General Hospital, Beijing 100853, China; Beijing Institute of Radiation Medicine, Beijing 100850, China*

Chao Tang − *Beijing Institute of Radiation Medicine, Beijing 100850, China*

Ju-Lei Zhang − *Department of Plastic and Reconstructive Surgery, The First Medical Centre, Chinese PLA General Hospital, Beijing 100853, China; Beijing Institute of Radiation Medicine, Beijing 100850, China*

Zhao-Yang Chen − *Department of Plastic and Reconstructive Surgery, The First Medical Centre, Chinese PLA General Hospital, Beijing 100853, China; Beijing Institute of Radiation Medicine, Beijing 100850, China*

Yan Li − *Department of Plastic and Reconstructive Surgery, The First Medical Centre, Chinese PLA General Hospital, Beijing 100853, China; Beijing Institute of Radiation Medicine, Beijing 100850, China*

Xiao-Jing Gong − *Department of Plastic and Reconstructive Surgery, The First Medical Centre, Chinese PLA General Hospital, Beijing 100853, China; Beijing Institute of Radiation Medicine, Beijing 100850, China*

Ming-Yi Qu − *Beijing Institute of Radiation Medicine, Beijing 100850, China*

Quan Zeng − *Beijing Institute of Radiation Medicine, Beijing 100850, China*

Ya-Li Jia − *Beijing Institute of Radiation Medicine, Beijing 100850, China*

Hai-Yang Wang − *Beijing Institute of Radiation Medicine, Beijing 100850, China*

Tao Fan − *Beijing Institute of Radiation Medicine, Beijing 100850, China*

https://doi.org/10.1021/acsnano.4c06921
ACS Nano 2024, 18, 26733−26750

Jing Ren − *Department of Plastic and Reconstructive Surgery, The First Medical Centre, Chinese PLA General Hospital, Beijing 100853, China*
Ling-Li Guo − *Department of Plastic and Reconstructive Surgery, The First Medical Centre, Chinese PLA General Hospital, Beijing 100853, China*
Jia-Fei Xi − *Beijing Institute of Radiation Medicine, Beijing 100850, China*
Xue-Tao Pei − *Beijing Institute of Radiation Medicine, Beijing 100850, China*

Complete contact information is available at:
https://pubs.acs.org/10.1021/acsnano.4c06921

Author Contributions

[‖]These authors contributed equally to this work. J.N.Z., W.Y., Y.H. and W.D.Y. conceived and designed the experiments. W.D.Y., J.N.Z., C.T., and J.L.Z. performed the experiments. W.D.Y., J.N.Z., C.T., J.L.Z., Z.Y.C., Y.L., X.J.G., M.Y. Q., Q.Z., Y.L.J., H.Y.W., T.F., J.R., L.L.G., J.F.X., X.T.P., Y.H., and W.Y. analyzed and discussed results. W.D.Y., J.N.Z., and W.Y. wrote the manuscript. All of the authors read and approved the manuscript.

Notes

The authors declare no competing financial interest.

ACKNOWLEDGMENTS

This work was financially supported by the Beijing Institute of Radiation Medicine.

ABBREVIATIONS

ADSCs, adipose-derived stem cells; MSCs, mesenchymal stem cells; FBS, fetal bovine serum; EV, extracellular vesicle; Met-EVs, metformin-treated ADSC-derived EVs; Ctrl-EVs, control EVs; DAM, decellularized adipose matrix; HAMA, hyaluronic acid methacrylic acid; MNP, microneedle patch; IR, irradiation; ROS, reactive oxygen species; mtROS, mitochondrial ROS; mtDNA, mitochondrial DNA; MTDR, MitoTracker deep red FM; Dil, 1,1′-dioctadecyl-3,3,3′,3′-tetramethylindocarbocyanine perchlorate; DAPI, 4′,6-diamidino-2-phenylindole; TEM, transmission electron microscopy; MS, mass spectrometry; SEM, scanning electron microscopy; HaCAT, human epidermal keratinocyte; HFF, human foreskin fibroblast; HUVECs, human umbilical vein endothelial cells; PBS, phosphate-buffered saline; CLSM, confocal laser scanning microscopy; ATP, adenosine 5′-triphosphate; NTA, nanoparticle tracking analysis; POD, postoperative day; Gy, gray; H&E, hematoxylin−eosin; IC_{50}, half maximal inhibitory concentration; ECM, extracellular matrix; MMP, $\Delta\Psi m$, mitochondrial membrane potential; DMEM, Dulbecco's Modified Eagle Medium

REFERENCES

(1) Behroozian, T.; Bonomo, P.; Patel, P.; Kanee, L.; Finkelstein, S.; van den Hurk, C.; Chow, E.; Wolf, J. R.; Behroozian, T.; Bonomo, P.; et al. Multinational Association of Supportive Care in Cancer (MASCC) Clinical Practice Guidelines for the Prevention and Management of Acute Radiation Dermatitis: International Delphi Consensus-Based Recommendations. *Lancet Oncol* **2023**, *24*, e172−e185.
(2) Du, Z.; Liu, H.; Huang, X.; Li, Y.; Wang, L.; Liu, J.; Long, S.; Li, R.; Xiang, Q.; Luo, S. Design and Synthesis of a Mitochondria-Targeting Radioprotectant for Promoting Skin Wound Healing Combined with Ionizing Radiation Injury. *Pharmaceuticals* **2022**, *15*, 721.
(3) Lintel, H.; Abbas, D. B.; Lavin, C. V.; Griffin, M.; Guo, J. L.; Guardino, N.; Churukian, A.; Gurtner, G. C.; Momeni, A.; Longaker, M. T.; Wan, D. C. Transdermal Deferoxamine Administration Improves Excisional Wound Healing in Chronically Irradiated Murine Skin. *J. Transl. Med.* **2022**, *20*, 274.
(4) Wang, Z.; Chen, Z.; Jiang, Z.; Luo, P.; Liu, L.; Huang, Y.; Wang, H.; Wang, Y.; Long, L.; Tan, X.; Liu, D.; Jin, T.; Wang, Y.; Wang, Y.; Liao, F.; Zhang, C.; Chen, L.; Gan, Y.; Liu, Y.; Yang, F.; et al. Cordycepin Prevents Radiation Ulcer by Inhibiting Cell Senescence *via* NRF2 and AMPK in Rodents. *Nat. Commun.* **2019**, *10*, 2538.
(5) Yu, C. Y.; Xu, H.; Ji, S.; Kwok, R. T.; Lam, J. W.; Li, X.; Krishnan, S.; Ding, D.; Tang, B. Z. Mitochondrion-Anchoring Photosensitizer with Aggregation-Induced Emission Characteristics Synergistically Boosts the Radiosensitivity of Cancer Cells to Ionizing Radiation. *Adv. Mater.* **2017**, *29*, 1606167.
(6) Averbeck, D.; Rodriguez-Lafrasse, C. Role of Mitochondria in Radiation Responses: Epigenetic, Metabolic, and Signaling Impacts. *Int. J. Mol. Sci.* **2021**, *22*, 11047.
(7) Zhang, Y. R.; Wang, J. Y.; Li, Y. Y.; Meng, Y. Y.; Zhang, Y.; Yang, F. J.; Xu, W. Q. Design and Synthesis a Mitochondria-Targeted Dihydronicotinamide As Radioprotector. *Free Radical Biol. Med.* **2019**, *136*, 45−51.
(8) Kim, J. H.; Jenrow, K. A.; Brown, S. L. Mechanisms of Radiation-Induced Normal Tissue Toxicity and Implications for Future Clinical Trials. *Rad. Oncol. J.* **2014**, *32*, 103−115.
(9) Xhuti, D.; Rebalka, I. A.; Minhas, M.; May, L.; Murphy, K.; Nederveen, J. P.; Tarnopolsky, M. A. The Acute Effect of Multi-Ingredient Antioxidant Supplementation Following Ionizing Radiation. *Nutrients* **2023**, *15*, 207.
(10) Luo, Z.; Yao, J.; Wang, Z.; Xu, J. Mitochondria in Endothelial Cells Angiogenesis and Function: Current Understanding and Future Perspectives. *J. Transl. Med.* **2023**, *21*, 441.
(11) McCully, J. D.; Del Nido, P. J.; Emani, S. M. Mitochondrial Transplantation for Organ Rescue. *Mitochondrion* **2022**, *64*, 27−33.
(12) Blitzer, D.; Guariento, A.; Doulamis, I. P.; Shin, B.; Moskowitzova, K.; Barbieri, G. R.; Orfany, A.; Del Nido, P. J.; McCully, J. D. Delayed Transplantation of Autologous Mitochondria for Cardioprotection in a Porcine Model. *Annal. Thoracic Surg.* **2020**, *109*, 711−719.
(13) Picone, P.; Porcelli, G.; Bavisotto, C. C.; Nuzzo, D.; Galizzi, G.; Biagio, P. L. S.; Bulone, D.; Di Carlo, M. Synaptosomes: New Vesicles for Neuronal Mitochondrial Transplantation. *J. Nanobiotechnol.* **2021**, *19*, 6.
(14) Ikeda, G.; Santoso, M. R.; Tada, Y.; Li, A. M.; Vaskova, E.; Jung, J. H.; O'Brien, C.; Egan, E.; Ye, J.; Yang, P. C. Mitochondria-Rich Extracellular Vesicles from Autologous Stem Cell-Derived Cardiomyocytes Restore Energetics of Ischemic Myocardium. *J. Am. Coll. Cardiol.* **2021**, *77*, 1073−1088.
(15) Zorova, L. D.; Kovalchuk, S. I.; Popkov, V. A.; Chernikov, V. P.; Zharikova, A. A.; Khutornenko, A. A.; Zorov, S. D.; Plokhikh, K. S.; Zinovkin, R. A.; Evtushenko, E. A.; Babenko, V. A.; Pevzner, I. B.; Shevtsova, Y. A.; Goryunov, K. V.; Plotnikov, E. Y.; Silachev, D. N.; Sukhikh, G. T.; Zorov, D. B. Do Extracellular Vesicles Derived from Mesenchymal Stem Cells Contain Functional Mitochondria? *Int. J. Mol. Sci.* **2022**, *23*, 7408.
(16) Liu, D.; Dong, Z.; Wang, J.; Tao, Y.; Sun, X.; Yao, X. The Existence and Function of Mitochondrial Component in Extracellular Vesicles. *Mitochondrion* **2020**, *54*, 122−127.
(17) Dutra Silva, J.; Su, Y.; Calfee, C. S.; Delucchi, K. L.; Weiss, D.; McAuley, D. F.; O'Kane, C.; Krasnodembskaya, A. D. Mesenchymal Stromal Cell Extracellular Vesicles Rescue Mitochondrial Dysfunction and Improve Barrier Integrity in Clinically Relevant Models of ARDS. *Eur. Res. J.* **2021**, *58*, 2002978.
(18) Morrison, T. J.; Jackson, M. V.; Cunningham, E. K.; Kissenpfennig, A.; McAuley, D. F.; O'Kane, C. M.; Krasnodembskaya, A. D. Mesenchymal Stromal Cells Modulate Macrophages in Clinically Relevant Lung Injury Models by Extracellular Vesicle Mitochondrial Transfer. *Am. J. Respir. Crit. Care Med.* **2017**, *196*, 1275−1286.

(19) Kim, J. M.; Kim, H.; Oh, S. H.; Jang, W. I.; Lee, S. B.; Park, M.; Kim, S.; Park, S.; Shim, S.; Jang, H. Combined Administration of Pravastatin and Metformin Attenuates Acute Radiation-Induced Intestinal Injury in Mouse and Minipig Models. *Int. J. Mol. Sci.* **2022**, *23*, 14827.
(20) Katila, N.; Bhurtel, S.; Park, P. H.; Choi, D. Y. Metformin Attenuates Rotenone-Induced Oxidative Stress and Mitochondrial Damage *via* the AKT/Nrf2 Pathway. *Neurochem. Int.* **2021**, *148*, 105120.
(21) Izzo, A.; Nitti, M.; Mollo, N.; Paladino, S.; Procaccini, C.; Faicchia, D.; Calì, G.; Genesio, R.; Bonfiglio, F.; Cicatiello, R.; Polishchuk, E.; Polishchuk, R.; Pinton, P.; Matarese, G.; Conti, A.; Nitsch, L. Metformin Restores the Mitochondrial Network and Reverses Mitochondrial Dysfunction in Down Syndrome Cells. *Hum. Mol. Genet.* **2017**, *26*, 1056−1069.
(22) Avcil, M.; Çelik, A. Microneedles in Drug Delivery: Progress and Challenges. *Micromachines* **2021**, *12*, 1321.
(23) Jovic, D.; Yu, Y.; Wang, D.; Wang, K.; Li, H.; Xu, F.; Liu, C.; Liu, J.; Luo, Y. A Brief Overview of Global Trends in MSC-Based Cell Therapy. *Stem Cell Rev. Rep.* **2022**, *18*, 1525−1545.
(24) Iannotta, D.; Yang, M.; Celia, C.; Di Marzio, L.; Wolfram, J. Extracellular Vesicle Therapeutics from Plasma and Adipose Tissue. *Nano Today* **2021**, *39*, 101159.
(25) O'Brien, C. G.; Ozen, M. O.; Ikeda, G.; Vaskova, E.; Jung, J. H.; Bayardo, N.; Santoso, M. R.; Shi, L.; Wahlquist, C.; Jiang, Z.; Jung, Y.; Zeng, Y.; Egan, E.; Sinclair, R.; Gee, A.; Witteles, R.; Mercola, M.; Svensson, K. J.; Demirci, U.; Yang, P. C. Mitochondria-Rich Extracellular Vesicles Rescue Patient-Specific Cardiomyocytes from Doxorubicin Injury: Insights into the SENECA Trial. *JACC. CardioOncol.* **2021**, *3*, 428.
(26) Mao, J.; Saiding, Q.; Qian, S.; Liu, Z.; Zhao, B.; Zhao, Q.; Lu, B.; Mao, X.; Zhang, L.; Zhang, Y.; Sun, X.; Cui, W. Reprogramming Stem Cells in Regenerative Medicine. *Smart Medicine* **2022**, *1*, No. e20220005.
(27) Cao, N.; Liao, T.; Liu, J.; Fan, Z.; Zeng, Q.; Zhou, J.; Pei, H.; Xi, J.; He, L.; Chen, L.; Nan, X.; Jia, Y.; Yue, W.; Pei, X. Clinical-Grade Human Umbilical Cord-Derived Mesenchymal Stem Cells Reverse Cognitive Aging *via* Improving Synaptic Plasticity and Endogenous Neurogenesis. *Cell Death Dis.* **2017**, *8*, No. e2996.
(28) Jia, Y.; Cao, N.; Zhai, J.; Zeng, Q.; Zheng, P.; Su, R.; Liao, T.; Liu, J.; Pei, H.; Fan, Z.; Zhou, J.; Xi, J.; He, L.; Chen, L.; Nan, X.; Yue, W.; Pei, X. HGF Mediates Clinical-Grade Human Umbilical Cord-Derived Mesenchymal Stem Cells Improved Functional Recovery in a Senescence-Accelerated Mouse Model of Alzheimer's Disease. *Adv. Sci.* **2020**, *7*, 1903809.
(29) Wang, Y.; An, H.; Liu, T.; Qin, C.; Sesaki, H.; Guo, S.; Radovick, S.; Hussain, M.; Maheshwari, A.; Wondisford, F. E.; O'Rourke, B.; He, L. Metformin Improves Mitochondrial Respiratory Activity through Activation of AMPK. *Cell Rep* **2019**, *29*, 1511−1523.e5.
(30) Xie, X.; Sinha, S.; Yi, Z.; Langlais, P. R.; Madan, M.; Bowen, B. P.; Willis, W.; Meyer, C. Role of Adipocyte Mitochondria In Inflammation, Lipemia And Insulin Sensitivity In Humans: Effects Of Pioglitazone Treatment. *Int. J. Obes.* **2018**, *42*, 213−220.
(31) Bogacka, I.; Xie, H.; Bray, G. A.; Smith, S. R. Pioglitazone Induces Mitochondrial Biogenesis in Human Subcutaneous Adipose Tissue *in Vivo*. *Diabetes* **2005**, *54*, 1392−1399.
(32) Neikirk, K.; Marshall, A. G.; Kula, B.; Smith, N.; LeBlanc, S.; Hinton, A., Jr. MitoTracker: a Useful Tool in Need of Better Alternatives. *Eur. J. Cell Biol.* **2023**, *102*, 151371.
(33) Li, X.; Gong, Y.; Li, D.; Xiang, L.; Ou, Y.; Jiang, L.; Shu, P.; Liu, X.; Guo, F.; Qin, D.; Mo, Z.; Qin, Q.; Wang, X.; Wang, Y. Low-Dose Radiation Therapy Promotes Radiation Pneumonitis by Activating NLRP3 Inflammasome. *Int. J. Radiat. Oncol., Biol., Phys.* **2020**, *107*, 804−814.
(34) Soltani, B.; Ghaemi, N.; Sadeghizadeh, M.; Najafi, F. Curcumin Confers Protection to Irradiated THP-1 Cells While Its Nano-formulation Sensitizes These Cells *via* Apoptosis Induction. *Cell Biol. Toxicol.* **2016**, *32*, 543−561.
(35) Guo, Y.; Chi, X.; Wang, Y.; Heng, B. C.; Wei, Y.; Zhang, X.; Zhao, H.; Yin, Y.; Deng, X. Mitochondria Transfer Enhances Proliferation, Migration, and Osteogenic Differentiation of Bone Marrow Mesenchymal Stem Cell and Promotes Bone Defect Healing. *Stem Cell Res. Ther.* **2020**, *11*, 245.
(36) Feng, Y.; Zhu, R.; Shen, J.; Wu, J.; Lu, W.; Zhang, J.; Zhang, J.; Liu, K. Human Bone Marrow Mesenchymal Stem Cells Rescue Endothelial Cells Experiencing Chemotherapy Stress by Mitochondrial Transfer *via* Tunneling Nanotubes. *Stem Cells Dev.* **2019**, *28*, 674−682.
(37) Qu, M.; Zou, X.; Fang, F.; Wang, S.; Xu, L.; Zeng, Q.; Fan, Z.; Chen, L.; Yue, W.; Xie, X.; Pei, X. Platelet-Derived Microparticles Enhance Megakaryocyte Differentiation and Platelet Generation *via* Mir-1915−3p. *Nat. Commun.* **2020**, *11*, 4964.
(38) Chen, Z.; Zhang, B.; Shu, J.; Wang, H.; Han, Y.; Zeng, Q.; Chen, Y.; Xi, J.; Tao, R.; Pei, X.; Yue, W.; Han, Y. Human Decellularized Adipose Matrix Derived Hydrogel Assists Mesenchymal Stem Cells Delivery and Accelerates Chronic Wound Healing. *J. Biomed. Mater. Res., Part A* **2021**, *109*, 1418−1428.
(39) Pu, W.; Han, Y.; Yang, M. Human Decellularized Adipose Tissue Hydrogels As a Culture Platform for Human Adipose-Derived Stem Cell Delivery. *J. Appl. Biomater. Funct. Mater.* **2021**, *19*, 228080002098814.
(40) Fan, L.; Zhang, X.; Wang, L.; Song, Y.; Yi, K.; Wang, X.; Zhang, H.; Li, L.; Zhao, Y. Bio-Inspired Porous Microneedles Dwelled Stem Cells for Diabetic Wound Treatment. *Adv. Funct. Mater.* **2024**, *34*, 2316742.
(41) Tan, H.; Ramirez, C. M.; Miljkovic, N.; Li, H.; Rubin, J. P.; Marra, K. G. Thermosensitive Injectable Hyaluronic Acid Hydrogel for Adipose Tissue Engineering. *Biomaterials* **2009**, *30*, 6844−6853.
(42) Seidlits, S. K.; Khaing, Z. Z.; Petersen, R. R.; Nickels, J. D.; Vanscoy, J. E.; Shear, J. B.; Schmidt, C. E. The Effects of Hyaluronic Acid Hydrogels with Tunable Mechanical Properties on Neural Progenitor Cell Differentiation. *Biomaterials* **2010**, *31*, 3930−3940.
(43) Suri, S.; Schmidt, C. E. Photopatterned Collagen-Hyaluronic Acid Interpenetrating Polymer Network Hydrogels. *Acta Biomater.* **2009**, *5*, 2385−2397.
(44) Spearman, B. S.; Agrawal, N. K.; Rubiano, A.; Simmons, C. S.; Mobini, S.; Schmidt, C. E. Tunable Methacrylated Hyaluronic Acid-Based Hydrogels As Scaffolds for Soft Tissue Engineering Applications. *Journal of biomedical materials research. Part A* **2020**, *108*, 279−291.
(45) Yao, S.; Chi, J.; Wang, Y.; Zhao, Y.; Luo, Y.; Wang, Y. Zn-MOF Encapsulated Antibacterial and Degradable Microneedles Array for Promoting Wound Healing. *Adv. Healthcare Mater.* **2021**, *10*, No. e2100056.
(46) Yuan, M.; Liu, K.; Jiang, T.; Li, S.; Chen, J.; Wu, Z.; Li, W.; Tan, R.; Wei, W.; Yang, X.; Dai, H.; Chen, Z. GelMA/PEGDA Microneedles Patch Loaded with HUVECs-Derived Exosomes and Tazarotene Promote Diabetic Wound Healing. *J. Nanobiotechnol.* **2022**, *20*, 147.
(47) Chen, P.; Zheng, L.; Wang, Y.; Tao, M.; Xie, Z.; Xia, C.; Gu, C.; Chen, J.; Qiu, P.; Mei, S.; Ning, L.; Shi, Y.; Fang, C.; Fan, S.; Lin, X. Desktop-Stereolithography 3D Printing of a Radially Oriented Extracellular Matrix/Mesenchymal Stem Cell Exosome Bioink for Osteochondral Defect Regeneration. *Theranostics* **2019**, *9*, 2439−2459.
(48) Murphy, C. M.; Haugh, M. G.; O'Brien, F. J. The Effect of Mean Pore Size on Cell Attachment, Proliferation and Migration in Collagen-Glycosaminoglycan Scaffolds for Bone Tissue Engineering. *Biomaterials* **2010**, *31*, 461−466.
(49) Zhang, X.; Lu, M.; Cao, X.; Zhao, Y. Functional Microneedles for Wearable Electronics. *Smart Med* **2023**, *2*, No. e20220023.
(50) Farhood, B.; Ashrafizadeh, M.; Khodamoradi, E.; Hoseini-Ghahfarokhi, M.; Afrashi, S.; Musa, A. E.; Najafi, M. Targeting of Cellular Redox Metabolism for Mitigation of Radiation Injury. *Life sciences* **2020**, *250*, 117570.
(51) Willenborg, S.; Sanin, D. E.; Jais, A.; Ding, X.; Ulas, T.; Nüchel, J.; Popović, M.; MacVicar, T.; Langer, T.; Schultze, J. L.; Gerbaulet, A.; Roers, A.; Pearce, E. J.; Brüning, J. C.; Trifunovic, A.; Eming, S. A. Mitochondrial Metabolism Coordinates Stage-Specific Repair Processes in Macrophages During Wound Healing. *Cell Metab.* **2021**, *33*, 2398−2414.e9.

https://doi.org/10.1021/acsnano.4c06921
ACS Nano 2024, 18, 26733−26750

(52) Eming, S. A.; Wynn, T. A.; Martin, P. Inflammation and Metabolism in Tissue Repair and Regeneration. *Science* **2017**, *356*, 1026−1030.
(53) Bai, Y.; Han, Y. D.; Yan, X. L.; Ren, J.; Zeng, Q.; Li, X. D.; Pei, X. T.; Han, Y. Adipose Mesenchymal Stem Cell-Derived Exosomes Stimulated by Hydrogen Peroxide Enhanced Skin Flap Recovery in Ischemia-Reperfusion Injury. *Biochem. Biophys. Res. Commun.* **2018**, *500*, 310−317.
(54) Horton, P.; Park, K. J.; Obayashi, T.; Fujita, N.; Harada, H.; Adams-Collier, C. J.; Nakai, K. WoLF PSORT: Protein Localization Predictor. *Nucleic Acids Res.* **2007**, *35*, W585−W587.
(55) Ma, J.; Chen, T.; Wu, S.; Yang, C.; Bai, M.; Shu, K.; Li, K.; Zhang, G.; Jin, Z.; He, F.; Hermjakob, H.; Zhu, Y. iProX: an Integrated Proteome Resource. *Nucleic Acids Res.* **2019**, *47*, D1211−D1217.
(56) Chen, T.; Ma, J.; Liu, Y.; Chen, Z.; Xiao, N.; Lu, Y.; Fu, Y.; Yang, C.; Li, M.; Wu, S.; Wang, X.; Li, D.; He, F.; Hermjakob, H.; Zhu, Y. iProX in 2021: Connecting Proteomics Data Sharing with Big Data. *Nucleic Acids Res.* **2022**, *50*, D1522−D1527.
(57) Rowland, M. B.; Moore, P. E.; Bui, C.; Correll, R. N. Assessing Wound Closure in Mice Using Skin-Punch Biopsy. *STAR Protoc.* **2023**, *4*, 101989.
(58) Varholick, J. A.; Godinez, G.; Jenkins, A.; Mobin, S.; Maden, M. Bite Wounds and Dominance Structures in Male and Female African Spiny Mice (Acomys Cahirinus): Implications for Animal Welfare and the Generalizability of Experimental Results. *Animals* **2024**, *14*, 64.
(59) Zhou, J. N.; Zhang, B.; Wang, H. Y.; Wang, D. X.; Zhang, M. M.; Zhang, M.; Wang, X. K.; Fan, S. Y.; Xu, Y. C.; Zeng, Q.; Jia, Y. L.; Xi, J. F.; Nan, X.; He, L. J.; Zhou, X. B.; Li, S.; Zhong, W.; Yue, W.; Pei, X. T. A Functional Screening Identifies a New Organic Selenium Compound Targeting Cancer Stem Cells: Role of c-Myc Transcription Activity Inhibition in Liver Cancer. *Liver Cancer. Adv. Sci.* **2022**, *9*, No. e2201166.

https://doi.org/10.1021/acsnano.4c06921
ACS Nano 2024, 18, 26733−26750